

OPEN ACCESS

A Time-Adaptive Order Reduction Technique for the Doyle-Fuller-Newman Electrochemical Model of Lithium-Ion Batteries

To cite this article: Eduardo Jané *et al* 2023 *J. Electrochem. Soc.* **170** 030539

View the [article online](#) for updates and enhancements.

You may also like

- [Physical Modelling of the Slow Voltage Relaxation Phenomenon in Lithium-Ion Batteries](#)
Toby L. Kirk, Colin P. Please and S. Jon Chapman
- [Comparison of Electrolyte Transport Modelling in Lithium-ion Batteries: Concentrated Solution Theory Vs Generalized Nernst-Planck Model](#)
Marco Lagnoni, Cristiano Nicoletta and Antonio Bertei
- [Dandelion v1: An Extremely Fast Solver for the Newman Model of Lithium-Ion Battery \(Dis\)charge](#)
Ivan Korotkin, Smita Sahu, Simon E. J. O'Kane et al.

Investigate your battery materials under defined force!
The new PAT-Cell-Force, especially suitable for solid-state electrolytes!



- Battery test cell for force adjustment and measurement, 0 to 1500 Newton (0-5.9 MPa at 18mm electrode diameter)
- Additional monitoring of gas pressure and temperature

www.el-cell.com +49 (0) 40 79012 737 sales@el-cell.com

EL-CELL[®]
electrochemical test equipment





A Time-Adaptive Order Reduction Technique for the Doyle-Fuller-Newman Electrochemical Model of Lithium-Ion Batteries

Eduardo Jané,^z Ruth Medeiros,^{id} Fernando Varas,^{id} and María Higuera^{id}

Departamento de Matemática Aplicada a la Ingeniería Aeroespacial—ETSIAE, Universidad Politécnica de Madrid, 28040 Madrid, Spain

A time-adaptive reduced order model (ROM) is developed for the electrochemical model for lithium-ion cells derived by Doyle, Fuller, and Newman (DFN) [M. Doyle, T. F. Fuller and J. Newman, *J. Electrochem. Soc.*, **140** 1526 (1993)]. The main advantage of a time-adaptive strategy is that it does not require a set of full order model simulations to be generated beforehand and, thus, it is the most cost-effective alternative when no databases are available. However, the reduction of this electrochemical problem exhibits special features that require ad hoc solutions, preventing the application of generic strategies. This complexity is carefully analysed, focusing on mode selection, treatment of non-linearities and error estimation. Despite of all this analysis being done for a pseudo-two-dimensional DFN model, we show that such complexity is intrinsic to the physics of the electrochemical problem, making the analysis applicable to a pseudo-four-dimensional DFN model, where results prove that the benefits of a reduction in the number of degrees of freedom are more self-evident. The efficiency, robustness and accuracy of our method are remarkable, as shown by the macroscopic (cell voltage) and internal (variable distributions) results obtained from the simulation of two different electrochemical cells under several charge/discharge C-rates.

© 2023 The Author(s). Published on behalf of The Electrochemical Society by IOP Publishing Limited. This is an open access article distributed under the terms of the Creative Commons Attribution Non-Commercial No Derivatives 4.0 License (CC BY-NC-ND, <http://creativecommons.org/licenses/by-nc-nd/4.0/>), which permits non-commercial reuse, distribution, and reproduction in any medium, provided the original work is not changed in any way and is properly cited. For permission for commercial reuse, please email: permissions@iopublishing.org. [DOI: [10.1149/1945-7111/acbc9b](https://doi.org/10.1149/1945-7111/acbc9b)]



Manuscript submitted September 16, 2022; revised manuscript received January 25, 2023. Published April 6, 2023.

List of Symbols

a	time-dependant mode amplitude
a_s	active material surface area to volume ratio, m^{-1}
c_e	lithium-ion concentration in the electrolyte, mol m^{-3}
c_s	lithium-ion concentration in the active particles, mol m^{-3}
$c_{s,\text{surf}}$	lithium-ion concentration at the surface of the active particles, mol m^{-3}
$c_{s,\text{surf},\text{max}}$	maximum lithium-ion concentration at the surface of the active particles, mol m^{-3}
D_e	lithium-ion diffusion coefficient in the electrolyte, $\text{m}^2 \text{s}^{-1}$
$D_{e,\text{eff}}$	effective lithium-ion diffusion coefficient in the electrolyte, $\text{m}^2 \text{s}^{-1}$
D_s	lithium-ion diffusion coefficient in the active particles, $\text{m}^2 \text{s}^{-1}$
F	Faraday constant, 96485 C mol^{-1}
g	time-dependant non-linearity mode amplitude
i_{app}	applied current per cell cross-sectional unit area, A m^{-2}
i_0	lithium-ion exchange current density, $\text{mol}(\text{m}^2 \text{s})^{-1}$
j_{Li}	lithium-ion exchange current density between active particles and electrolyte, $\text{mol}(\text{m}^2 \text{s})^{-1}$
k_0	lithium-ion exchange kinetic constant, $\text{m}^{4-3\alpha}/(\text{mol}^{1-\alpha} \text{s})$
L	cell thickness, m
L_a	anode thickness, m
L_c	cathode thickness, m
L_s	separator thickness, m
r^*	non-dimensional radial coordinate of the active particles
R	universal gas constant, $8.314 \text{ J}(\text{mol K})^{-1}$
R_s	active particle radius, m
S	cross-sectional area, m^2
t	time, s
t_+^0	ionic transference number
T	cell temperature, K
U_{ocv}	open-circuit voltage, V
x	cell thickness coordinate
X	snapshots matrix
α	cathodic charge transfer coefficient, 0.5
β	non-linear function

γ	Bruggeman exponent
ε	relative error
$\hat{\varepsilon}$	relative error estimator
ε_e	porosity
$\varepsilon_{\hat{\varepsilon}}$	relative ROM error estimator tolerance
ε_{svd}	relative SVD truncation tolerance
η	overpotential, V
κ	ionic conductivity, S m^{-1}
κ_{eff}	effective ionic conductivity, S m^{-1}
$\kappa_{D,\text{eff}}$	effective ionic diffusion-conductivity, A m^{-1}
ξ	non-linearity mode shape
Ξ	matrix of non-linearity mode shapes
σ	singular value
σ_{eff}	effective electronic conductivity, S m^{-1}
ϕ_e	electric potential of the electrolyte phase, V
ϕ_s	electric potential of the solid phase, V
$\chi_{t,0}^{\text{fom}}$	initial full order model simulation time fraction
$\chi_{t,0}^{\text{rom}}$	intermediate full order model simulation time fraction of the initial full order model simulation time fraction
χ_t^{rom}	maximum reduced order model simulation time fraction
$\chi_{t,0}^{\text{rom}}$	initial reduced order model simulation time fraction
ψ	mode shape
Ψ	matrix of mode shapes

Across a rapidly growing range of engineering applications, battery-powered electric devices are becoming a realistic and competitive alternative to those relying on traditional energy sources like combustion. This is due to important improvements in the performance of electrochemical cells arising, in part, from better design tools, and specially those based on numerical models, aimed at optimising energy storage and achieving safe charge/discharge cycles and increasing the battery lifetime, among other objectives. Understanding and conceiving good design tools requires accurate first-principle electrochemical models that are capable of describing not only the output voltage given by the cell, but also the internal electrochemical state of the battery during the charge/discharge process.

A good model should accurately predict the performance and lifetime of the battery cell, reveal its important mechanisms, describe its main electrochemical processes and indicate how to achieve optimal performance. In particular, physics-based models that

^zE-mail: eduardo.jane.soler@upm.es

account for the complex electrode microstructures can capture microscopic effects in detail and are able to describe ion dynamics in the electrodes.^{1,2} Some of these models also include degradation effects, which influence both the local and global behavior of lithium-ion cells.³ Although they are capable of providing accurate results in three-dimensional microstructures, microscale models can be very computationally demanding (a typical time for a simulation run is about 15 h on a single cluster core⁴) and can only be used to simulate relatively small volumes within the electrodes. Therefore, microscale models are infeasible for systematically optimising the design and control of batteries through a series of simulations performed while varying parameters.

Numerical optimisation tasks require reduced macroscale models that bypass the complexity of the electrode while capturing the relevant physics of the microscale. Such continuum-scale first-principle models are obtained, in essence, from averaging the system of microscale equations over volume. The Doyle-Fuller-Newman (DFN) model⁵ is, arguably, the most widely used in this field for the analysis and control of charging/discharging battery cells and packs. This approach assumes the one-dimensional transport (along the cell thickness) of lithium-ions in the electrolyte, with the electrode active materials being made up of homogeneously distributed spherical particles of the same average size, in which lithium transport occurs via diffusion in the direction normal to their surface; they are therefore also known as pseudo-two-dimensional (p2D) models. The numerical solution of the p2D DFN model provides very useful insights on the electrochemical dynamics of the cell. Nevertheless, if a cell/battery design is to be optimised, a more detailed description is needed and cell utilization heterogeneities (along the other cell dimensions) must be captured. The DFN model itself can be easily extended to consider a three-dimensional cell (leading to a pseudo-four-dimensional, or p4D, model), but the computational cost of numerically solving this model is extremely high since suitable meshes will contain several million degrees of freedom (DOFs). Even the cell optimisation based on a p2D DFN model can be computationally expensive if a large number of cell simulations (as typically required during optimisation) are needed.

Motivated by these difficulties, considerable effort has been directed toward the development of reduced models that can provide accurate results in real time, and that may also be used for control and optimisation purposes. The majority of these models rely on simplifications of a p2D model through homogenised lithium-ion transport along the electrodes, such as the well-known Single Particle model of Refs. 6, 7, or on the efficient treatment of non-linearities^{8–11} (and references therein). Alternative approaches to reducing their computational cost include reduced order models (ROMs) derived using Galerkin projections based on orthogonal polynomials.^{12,13} In all of these published works, the reduction techniques were applied to previously simplified p2D models and, therefore, the models are only expected to be accurate in certain limiting cases. A ROM using a proper orthogonal decomposition (POD) was first derived from the complete p2D DFN model in Ref. 14. The obtained results were accurate for moderate applied current rates (less than 4C). However, the acceleration factor with respect to the numerical integration of the full order model (FOM), of about 7, was lower than expected considering the great reduction in the number of DOFs that was achieved (from 14580 to 200). This was partly due to the non-linearities that required to reconstruct the state variables at every iteration of the solver. In Ref. 15, the discrete empirical interpolation method (DEIM) is applied to the non-linear terms and the computational cost is reduced by an additional factor ranging from 2 to 18, depending on the charge/discharge process considered. The greater the reduction in DOFs of the problem, the higher the acceleration factor that may be achieved. Thus, in Ref. 16 a ROM based on a collocation method with Chebyshev polynomials improved computation time by a factor of 20 to 50 as compared with the finite elements model describing the electrochemical processes in the electrodes, coupled to the electrothermal effects occurring in the

two-dimensional current collectors. The speed-up factor achieved in a POD-DEIM ROM applied to a full microscale model may reach a factor of 120.⁴

Using the techniques described above, the electrochemical cell simulation using a ROM can be significantly accelerated when compared to the simulation using the original numerical model. However, this fact cannot hide that a large computational effort must be done in order to prepare the ROM. In particular, the FOM must be solved many times in order to setup a numerical solution database from which information to build the ROM is extracted. The size of such database strongly influences the performance of the derived ROM. With cell optimisation in mind, this solution database should conveniently cover all the design parameter space. The generation of such database can then involve a huge computational cost and, although cell optimisation itself (using the derived ROM) is significantly accelerated, the whole optimisation process (including ROM preparation) may result unaffordable.

The above mentioned difficulty is shared by any pre-processed ROM. In order to overcome this severe drawback, a time-adaptive ROM could be considered. Under this approach,¹⁷ no database is required and the information from the original numerical model is instead extracted using an on-the-fly technique. The numerical solution using the original FOM is computed along some time periods during the cell simulation and a ROM is built using the information provided by such solution. An error estimation for the ROM solution can also be implemented in order to detect if more information (from the original FOM) is needed in order to improve the ROM, and an update algorithm is used to derive a new ROM combining all the available information. With such adaptive ROM technique, the speed-up of a cell simulation can be moderate (it will be bounded by the fraction of time the full numerical model is used to simulate the cell performance) but, since no database is needed, the overall reduction of the computational effort can be very significantly improved in comparison with pre-processed ROM techniques. The comparative advantage of this time-adaptive ROM strategy can be understood considering a simple scenario in which a pre-processed ROM is used during cell design, where 5 cell design parameters are taken and 20 different cell selections are analysed. Calling t_{FOM} the computational time for a single FOM simulation and assuming an acceleration factor of $f_{p-p} = 20$ (as presented in Ref. 15) for the pre-processed ROM, the initial cost of exploring the design parameter space taking only 4 values for each parameter using the FOM would be $4^5 \cdot t_{FOM} = 1024 \cdot t_{FOM}$. Thus, the total computational time to analyze the 20 cell selections using the pre-processed ROM approach would be $(1024 + 20/f_{p-p}) \cdot t_{FOM} = 1025 \cdot t_{FOM}$. The time-adaptive ROM strategy presented in this manuscript can achieve acceleration factors of $f_{t-a} \sim 10$ (as it is shown later in this text), but a more conservative speed-up factor of $f'_{t-a} = 4$ can be considered. In this case, the analysis of 20 cells would only require a computational time of $(20/f'_{t-a}) \cdot t_{FOM} = 5 \cdot t_{FOM}$, resulting 205 times cheaper than the pre-processed approach. Hence, the use of a time-adaptive strategy is a more suitable way to assess cell design optimisation problems, particularly using p4D DFN models, which would otherwise require vast computational resources.

The goal of this paper is to explore the application of time-adaptive ROMs to the solution of the DFN model, adapting some ideas from Ref. 17. Several difficulties must be overcome in order to extend such ideas from a single partial differential equation to a complex system of partial differential equations. Those difficulties are mainly related to mode selection, treatment of non-linear terms, solution stability and error estimates. Finally, although the aim of such acceleration techniques is the solution of p4D DFN models, for the sake of simplicity the discussion is done using the p2D DFN model.

The remainder of this paper is organised as follows. First, the p2D DFN model is presented in its variational form, introducing the general characteristics of the function space in which the ROM

solution will be found. Then, the time-adaptive ROM is described, emphasising on its formulation, the selection of an appropriate basis for the function space of its solution, the solvability and numerical stability of the resulting system of equations, error estimation and the adopted time-adaptive strategy. Next, results of the proposed time-adaptive ROM are shown for two different electrochemical cells, both consisting of graphite (G) anodes in combination with lithium nickel manganese cobalt oxide (NMC) and lithium iron phosphate (LFP) cathodes, under various charge/discharge rate scenarios (including a hybrid load cycle) of up to 5C. Additionally, results of a p4D time-adaptive ROM implementation are presented to further justify the validity of the analysis carried out using the p2D model. Finally, conclusions are derived from the analysis of the proposed model and its performance.

Model for a Lithium-ion Battery Cell. Variational Formulation

The model considered in this work is a p2D DFN model, consisting in a system of nonlinear partial differential equations describing the one-dimensional dynamics for electric charge in the solid phase and ionic charge and mass transport in the electrolyte phase along the cell thickness (x), as well as mass transport within the solid phase, which is represented in each electrode by homogeneously distributed spherical particles (with radial coordinate r) of the same radius R_s (see Fig. 1). A brief summary of the governing equations and their corresponding boundary conditions is given in Table I. We refer the interested reader to Ref. 5 for more detail.

Regarding the equation describing charge conservation in the solid phase, note that in addition to the boundary conditions imposed on the flux of solid phase potential, ϕ_s , a reference value must be set (for instance $\phi_s|_{x=0} = 0$ can be imposed, but other alternatives are also used in practice) for the equation to have a unique solution.

The numerical implementation of the full electrochemical p2D model is carried out using the finite element method (FEM), which requires defining the weak (or variational) form of the system of equations. In order to obtain the variational formulation of a system of PDEs (see, for example, Ref. 18), each equation has to be multiplied by a test function v lying in some Sobolev space V and then integrated over the corresponding domain Ω , performing integration by parts on the terms with second-order derivatives and taking into account the boundary conditions of the problem. After some algebra, the variational form of the p2D DFN system results in the following expressions:

- Charge conservation in the solid phase,

$$\int_{\Omega} \sigma_{eff} \frac{\partial \phi_s}{\partial x} \frac{dv}{dx} dx + \int_{\Omega} a_s F j_{Li} v dx = -i_{app} v|_{x=L}. \quad [1]$$

- Mass conservation in the solid phase,

$$\begin{aligned} \int_{\Omega} \int_{\Omega_{r^*}} r^{*2} \frac{\partial c_s}{\partial t} v dr^* dx + \int_{\Omega} \int_{\Omega_{r^*}} \frac{1}{R_s^2} D_s r^{*2} \frac{\partial c_s}{\partial r^*} \frac{\partial v}{\partial r^*} dr^* dx \\ + \int_{\Omega} \frac{1}{R_s} j_{Li} v|_{r^*=1} dx = 0. \end{aligned} \quad [2]$$

- Charge conservation in the electrolyte phase,

$$\int_{\Omega} \left(\kappa_{eff} \frac{\partial \phi_e}{\partial x} + \kappa_{D,eff} \frac{\partial \ln c_e}{\partial x} \right) \frac{dv}{dx} dx - \int_{\Omega} a_s F j_{Li} v dx = 0. \quad [3]$$

- Mass conservation in the electrolyte phase,

$$\begin{aligned} \int_{\Omega} \frac{\partial (\varepsilon_e c_e)}{\partial t} v dx + \int_{\Omega} D_{e,eff} \frac{\partial c_e}{\partial x} \frac{dv}{dx} dx \\ - \int_{\Omega} a_s (1 - t_+^0) j_{Li} v dx = 0. \end{aligned} \quad [4]$$

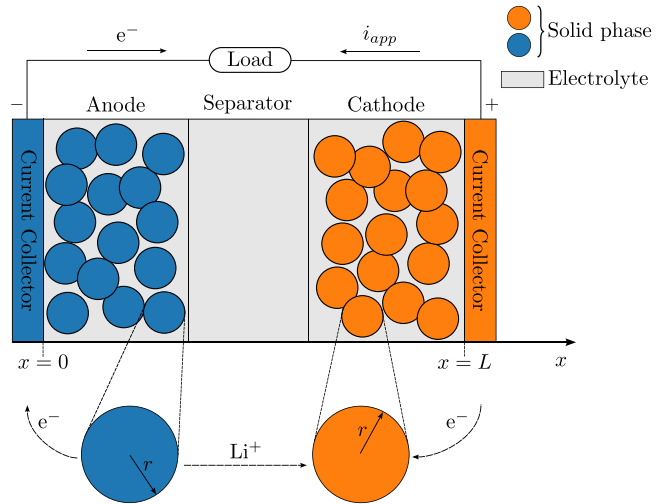


Figure 1. Scheme of a p2D cell model.

- Butler-Volmer kinetics,

$$\int_{\Omega} j_{Li} v dx = \int_{\Omega} f_{j_{Li}} v dx. \quad [5]$$

Since mass conservation in the solid phase (see Table I) introduces the pseudo-dimension r , the variational form in Eq. 2, which has been written using the non-dimensional radial coordinate $r^* = r/R_s$, requires the integration along the domains $\Omega_{r^*} = [0, 1]$ and Ω using the test function $v(x, r^*) \in H^1(\Omega \times \Omega_{r^*})$. Note that the lithium-ion exchange current density, j_{Li} , is considered as a problem variable, which simplifies the extension of this model to include solid-electrolyte interphase (SEI) formation phenomena.

The variational problem formed by Eqs. 1–5 is continuous and defines the solution $\mathbf{u}(x, r^*, t) = \{\phi_s(x, t), c_s(x, r^*, t), \phi_e(x, t), c_e(x, t), j_{Li}(x, t)\}$ in a infinite dimensional function space, as in the original problem. However the continuity requirements of u in the variational problem are weaker, which has practical consequences as the use of piecewise continuous polynomial function spaces. Thus, the finite element method finds an approximate solution of 1–5 in a discrete (finite-dimensional) function space V_h , a subspace of the infinite dimensional function space V in the variational problem. Since the Galerkin method will also be used in the derivation of the ROM, a second function space \hat{V}_h will be built. Such function space \hat{V}_h will be, in turn, a subspace of V_h with, hopefully, a much smaller dimension.

Time-Adaptive ROM

This Section is devoted to the derivation of a time-adaptive ROM from the electrochemical problem 1–5, starting with the formulation of the ROM, addressing its solvability and error estimation, and finally defining the adopted time-adaptive strategy.

ROM formulation.—The proposed ROM is based on the Galerkin method. Thus, the variational form previously described is used and only the function space \hat{V}_h must be specified. In order to build this space, the well known POD method is used. Here we just summarise the main results of this technique, referring the reader to Ref. 19 and references therein, for a detailed description of the method.

The procedure starts by finding a low-dimensional set of basis functions in the L^2 -Hilbert space, that contain the relevant dynamics of the FOM. Following the snapshot method,²⁰ first we consider the set of snapshots which may be given by the solution of the full problem (or other data sets) at N instants of time,

Table I. Electrochemical p2D DFN model.⁵

Description	Equation	Boundary conditions
Charge conservation in the solid phase, ϕ_s	$\frac{\partial}{\partial x} \left(\sigma_{eff} \frac{\partial \phi_s}{\partial x} \right) = a_s F j_{Li}$	$\phi_s _{x=0} = 0$ $\sigma_{eff} \frac{\partial \phi_s}{\partial x} \Big _{x=L} = -i_{app}(t)$ $\sigma_{eff} \frac{\partial \phi_s}{\partial x} \Big _{x=L_a} = \sigma_{eff} \frac{\partial \phi_s}{\partial x} \Big _{x=L_c} = 0$
Mass conservation in the solid phase, c_s	$\frac{\partial c_s}{\partial t} = \frac{1}{r^2} \frac{\partial}{\partial r} \left(D_s r^2 \frac{\partial c_s}{\partial r} \right)$	$D_s \frac{\partial c_s}{\partial r} \Big _{r=R_s} = -j_{Li}$ $D_s \frac{\partial c_s}{\partial r} \Big _{r=0} = 0$
Charge conservation in the electrolyte phase, ϕ_e	$\frac{\partial}{\partial x} \left(\kappa_{eff} \frac{\partial \phi_e}{\partial x} + \kappa_{D,eff} \frac{\partial \ln c_e}{\partial x} \right) = -a_s F j_{Li}$	$\left(\kappa_{eff} \frac{\partial \phi_e}{\partial x} + \kappa_{D,eff} \frac{\partial \ln c_e}{\partial x} \right) \Big _{x=0} = 0$ $\left(\kappa_{eff} \frac{\partial \phi_e}{\partial x} + \kappa_{D,eff} \frac{\partial \ln c_e}{\partial x} \right) \Big _{x=L} = 0$
Mass conservation in the electrolyte phase, c_e	$\frac{\partial(\varepsilon_e c_e)}{\partial t} = \frac{\partial}{\partial x} \left(D_{e,eff} \frac{\partial c_e}{\partial x} \right) + a_s (1 - t_+^0) j_{Li}$	$\frac{\partial c_e}{\partial x} \Big _{x=0} = \frac{\partial c_e}{\partial x} \Big _{x=L} = 0$
Butler-Volmer kinetics, j_{Li}	$j_{Li} = f_{j_{Li}}(\phi_s, \phi_e, c_s, c_e) \text{ with } f_{j_{Li}}(\phi_s, \phi_e, c_s, c_e) = i_0 \left[\exp\left(\frac{(1-\alpha)F}{RT}\eta\right) - \exp\left(-\frac{\alpha F}{RT}\eta\right) \right]$ $i_0 = k_0 c_e^{(1-\alpha)} c_{s,surf}^\alpha (c_{s,surf,max} - c_{s,surf})^{1-\alpha}$ $\eta = \phi_s - \phi_e - U_{ocv}(c_s)$	

$$\begin{aligned} u_1(x) &= u(x, t_1), \quad u_2(x) = u(x, t_2), \dots, \\ u_N(x) &= u(x, t_N). \end{aligned} \quad [6]$$

Then, the so-called POD-modes can be efficiently computed from the thin or economy-sized singular value decomposition (SVD) of the snapshots matrix $X = [\mathbf{u}_1, \dots, \mathbf{u}_N] \in \mathbb{R}^{M \times N}$, where the columns \mathbf{u}_k correspond to distributions of M -nodal values along the spatial coordinates of a variable (or a non-linearity) over N time steps, generally having $M \gg N$. Thus, the SVD of X can be written as

$$X = \Psi \Sigma \Phi^T, \quad [7]$$

where the columns of the matrices $\Psi \in \mathbb{R}^{M \times N}$ and $\Phi \in \mathbb{R}^{N \times N}$ are the (economy-sized, assuming $N < M$) left and right singular vectors of X , respectively. The matrix $\Sigma \in \mathbb{R}^{N \times N}$ is a diagonal matrix and its elements, called singular values, are sorted in descending way as,

$$\sigma_1 \geq \dots \geq \sigma_n \geq \dots \geq \sigma_N \geq 0. \quad [8]$$

A truncation of the Ψ matrix,

$$\Psi_n = [\psi_1, \dots, \psi_n], \quad \text{where } n \ll N,$$

can be defined, containing only the left singular vectors associated to the n largest singular values and providing an orthonormal basis that gives a low-dimensional representation of the snapshot data. As shown in Ref. 19 (and references therein), POD-modes provide the best approximation of the snapshots 6, among all expansions with n terms, minimising the root-mean-squared error when reconstructing the N snapshots after truncations to n . Thus, the accuracy of the approximation is directly related with the number modes ψ_n that are considered and their corresponding singular values σ_n , which measure the relevance of such modes in the dynamics defined by the snapshots.

The solution of the FOM can now be projected onto the POD manifold (using the L^2 -inner product) to obtain,

$$\begin{aligned} u(x, t) &\simeq \hat{u}^h(x, t) = \sum_{j=1}^n a_j(t) \psi_j(x), \quad \text{with} \\ a_j &= (u, \psi_j) = \int_{\Omega} u(x, t) \psi_j(x) dx, \end{aligned} \quad [9]$$

where the coefficients $a_j(t)$ are called amplitudes of the modes. Note that \hat{u}^h belongs to the function space $\hat{V}_h = \{\psi_j\}_{j=1, \dots, n}$, which is a subspace of the function space V_h defined by the FEM in order to solve 1–5.

Thus, applying the snapshot method described above to the solution of the electrochemical model in Table I, we obtain the associated POD manifold and the following expansions for the variables of the problem are considered:

$$\begin{aligned} \phi_s(x, t) &\simeq \hat{\phi}_s^h(x, t) = \sum_{i=1}^{N_{\phi_s}} a_i^{\phi_s}(t) \psi_i^{\phi_s}(x) \\ &= \Psi_{\phi_s}(x) \mathbf{a}_{\phi_s}(t), \end{aligned} \quad [10a]$$

$$\begin{aligned} c_s(x, r^*, t) &\simeq \hat{c}_s^h(x, r^*, t) = \sum_{i=1}^{N_{r^*}} a_i^{r^*}(x, t) \psi_i^{r^*}(r^*) \\ &= \sum_{i=1}^{N_{r^*}} \left(\sum_{j=1}^{N_{c_s}} a_j^{c_s}(t) \psi_{ij}^{c_s}(x) \right) \psi_i^{r^*}(r^*) \\ &= T_{c_s}(x, r^*) \otimes \mathbf{a}_{c_s}(t), \end{aligned} \quad [10b]$$

$$\begin{aligned} \phi_e(x, t) &\simeq \hat{\phi}_e^h(x, t) = \sum_{i=1}^{N_{\phi_e}} a_i^{\phi_e}(t) \psi_i^{\phi_e}(x) \\ &= \Psi_{\phi_e}(x) \mathbf{a}_{\phi_e}(t), \end{aligned} \quad [10c]$$

$$c_e(x, t) \simeq \hat{c}_e^h(x, t) = \sum_{i=1}^{N_{c_e}} a_i^{c_e}(t) \psi_i^{c_e}(x) = \Psi_{c_e}(x) \mathbf{a}_{c_e}(t), \quad [10d]$$

$$j_{Li}(x, t) \simeq \hat{j}_{Li}^h(x, t) = \sum_{i=1}^{N_{j_{Li}}} a_i^{j_{Li}}(t) \psi_i^{j_{Li}}(x) = \Psi_{j_{Li}}(x) \mathbf{a}_{j_{Li}}(t). \quad [10e]$$

In order to solve c_s along the non-dimensional form of the pseudo-dimension, r^* , the proposed FOM uses a pseudo-spectral method based on even order Legendre polynomials, which already constitutes a significant reduction in DOFs with respect to the system that would result of applying the finite element method. Thus, the same Legendre polynomials are also used when building the ROM to describe c_s , denoted as $\psi_i^{r^*}(r^*)$ with $i = 1, \dots, N_{r^*}$. T_{c_s} is a three-dimensional tensor containing the set of $\psi_i^{r^*}$ Legendre polynomials and $\psi_{i,j}^{c_s}$ modes, which are obtained by performing a single SVD on a snapshots matrix formed by all $a_i(x, t)$ Legendre polynomial coefficients, where the distributions along x of each coefficient are concatenated in every column. This SVD results in a single set of N_{c_s} modes to represent all the coefficients, which can be handled separately (undoing the concatenation of their components and leading to $\psi_{N_{r^*} \times N_{c_s}}^{c_s}$ modes) in the ROM implementation but will share the same time-dependant amplitudes $a_j^{c_s}(t)$ with $j = 1, \dots, N_{c_s}$ when performing the Galerkin projection. The system of equations that has to be solved to obtain the amplitude vectors, $\mathbf{a}_{\phi_s}(t)$, $\mathbf{a}_{c_s}(t)$, $\mathbf{a}_{\phi_e}(t)$, $\mathbf{a}_{c_e}(t)$, and $\mathbf{a}_{j_{Li}}(t)$, results from applying a POD-Galerkin projection to the system of governing equations shown in Table I. The obtained ROM is given by a system of differential algebraic equations,

$$K_{\phi_s} \mathbf{a}_{\phi_s} + A_{\phi_s}^{j_{Li}} \mathbf{a}_{j_{Li}} = \mathbf{b}_{\phi_s}(t) \quad [11a]$$

$$M_{c_s} \frac{d\mathbf{a}_{c_s}}{dt} + K_{c_s} \mathbf{a}_{c_s} + A_{c_s}^{j_{Li}} \mathbf{a}_{j_{Li}} = 0 \quad [11b]$$

$$K_{\phi_e} \mathbf{a}_{\phi_e} + B_{\phi_e}^{c_e} \hat{\beta}_{c_e}^h(\mathbf{a}_{c_e}) + A_{\phi_e}^{j_{Li}} \mathbf{a}_{j_{Li}} = 0 \quad [11c]$$

$$M_{c_e} \frac{d\mathbf{a}_{c_e}}{dt} + K_{c_e} \mathbf{a}_{c_e} + A_{c_e}^{j_{Li}} \mathbf{a}_{j_{Li}} = 0 \quad [11d]$$

$$K_{j_{Li}} \mathbf{a}_{j_{Li}} + B_{j_{Li}}^{j_{Li}} \hat{\beta}_{j_{Li}}^h(\mathbf{a}_{\phi_s}, \mathbf{a}_{c_s}, \mathbf{a}_{\phi_e}, \mathbf{a}_{c_e}) = 0. \quad [11e]$$

For the sake of brevity, only the non-linear terms of the system $\hat{\beta}_{c_e}^h$ and $\hat{\beta}_{j_{Li}}^h$ are detailed in this text, while the matrices involved in the linear part of the expressions are given in Appendix A.

Since the time integration of the p2D ROM is performed using an implicit Euler method, the non-linearities present in the model imply that a non-linear system has to be solved in each time step. In order to capture more accurately the non-linear dynamics of the problem, every non-linearity is represented by a specific set of POD-modes ξ_i , obtained via the truncated SVD of the snapshots matrix of the corresponding non-linearity (computed using the FOM solution). Therefore, the non-linearities are approximated as follows,

$$\begin{aligned} \frac{\partial \ln c_e}{\partial x} &= \frac{1}{c_e} \frac{\partial c_e}{\partial x} = \beta_{c_e}(x, t) \simeq \hat{\beta}_{c_e}^h(x, t) \\ &= \sum_{i=1}^{N_{\beta_{c_e}}} g_i^{c_e}(t) \xi_i^{c_e}(x) = \Xi_{c_e}(x) \mathbf{g}_{c_e}(t), \end{aligned}$$

$$\begin{aligned} f_{j_{Li}} &= \beta_{j_{Li}}(x, t) \simeq \hat{\beta}_{j_{Li}}^h(x, t) \\ &= \sum_{i=1}^{N_{\beta_{j_{Li}}}} g_i^{j_{Li}}(t) \xi_i^{j_{Li}}(x) = \Xi_{j_{Li}}(x) \mathbf{g}_{j_{Li}}(t). \end{aligned}$$

The system of non-linear equations is solved using the Newton method, which requires the computation of non-linearities as well as their derivatives in each iteration and at every node of the discretised domain. These calculations represent the main computational bottleneck when solving the ROM. Therefore, the DEIM is used to interpolate the non-linearities and their derivatives from a set of pre-selected DEIM points, x_k , to the rest of the domain, having the general form

$$\begin{aligned} \tilde{\beta}(x_k, t) &\simeq \hat{\beta}^h(x_k, t) = \sum_{i=1}^{N_{\beta}} g_i(t) \tilde{\xi}_i(x_k) \\ &= \tilde{\Xi}(x_k) \mathbf{g}(t), \end{aligned}$$

$$\hat{\beta}^h(x, t) = \Xi(x) \mathbf{g}(t) \simeq \Xi(x) \tilde{\Xi}^{-1}(x_k) \hat{\beta}^h(x_k, t),$$

where tilde symbol \sim denotes evaluation of the given expression, vector or matrix at the x_k DEIM points. This technique is applied in pre-processed ROMs (see, for instance, Ref. 15) in order to significantly reduce the computational cost of the ROM integration. Since most electrolyte transport properties are concentration-dependent, many other non-linearities can arise in the DFN model. Taking into account that treatment of such non-linearities is exactly the same and the qualitative behavior of the resulting ROM is not affected, those non-linearities have been neglected in this work for the sake of simplicity.

Following this procedure, the selection of the POD-modes is straightforward once the low-rank truncation of the left singular vector matrices that result from the computations of SVDs is done. The simple approach to select the number of modes, n_1 , that is commonly used to describe a given variable (or non-linearity) in the ROM consists of the definition of a tolerance ϵ_{svd} such that

$$n_1 = \min_{1 \leq i \leq N} \left\{ i \mid \left| \frac{\sigma_i}{\sigma_1} \right| < \epsilon_{svd} \right\}. \quad [12]$$

The value of this tolerance is directly related to the precision with which the complete set of N snapshots can be reconstructed using the n_1 modes resulting from the truncation of the SVD. Nevertheless, the electrochemical cell model exhibits special features which make essential to conduct the modes selection more carefully.

Selection of POD-modes.—This Section is devoted to highlighting the main characteristics of the electrochemical p2D model that prevent the use of a standard SVD truncation 12 to get the minimum number of modes required to describe the dynamics of the system with sufficient accuracy. For the sake of clarity, our discussion is built around a *baseline case* corresponding to a 0.5C full discharge of a G-NMC cell. Additionally, to demonstrate the robustness of the method, results corresponding to a G-LFP cell will also be shown.

The parameter values necessary to build the electrochemical models of both cells are given in Tables B-1 and B-2 of Appendix B. Regarding the discretisation of the cell domain for both FOM and ROM, each subdomain (anode, separator and cathode) is formed by 30 P1 elements (with linear functions as basis functions and their nodes as DOFs) of the same size, thus having a total of 91 nodes. In all results shown in this work, the numbering for both elements and nodes starts at 0 and increases along the x axis following the cell arrangement depicted in Fig. 1.

Now, we start by noticing that using the first singular value as a reference to decide the number of modes to be might lead to an insufficient representation of some of the variables, since the value of σ_1 is related to the order of magnitude of the data in the snapshots, while the values $\sigma_2, \sigma_3, \dots, \sigma_n$ are related to the order of the fluctuations around the mean field that their corresponding modes represent. Therefore, a very fast initial decay in the singular values can be observed for variables whose solution exhibits relatively small fluctuations around their mean values, such as ϕ_s and c_e . However, these fluctuations may be relevant to the solution of the system and therefore require a sufficiently accurate representation in the ROM set of modes. Moreover, the fact that the modes are extracted from snapshot matrices that contain the solution of the FOM along various domains, where the order of magnitude of the variables of the problem might differ significantly, can also imply that the first modes contain more information about the solution on the subdomain with a greater average value.

Such behavior, typically observed in the modes extracted for ϕ_s when the anode and cathode materials have different open circuit voltage (OCV) characteristic values and/or capacities, is shown in Fig. 2, where the fourth singular value drops by over 6 orders of magnitude with respect to the first one (Fig. 2a) and the first four modes exhibit small perturbations around the mean value for ϕ_s in the anode (distinguishable in Fig. 2b only for the third mode and above).

Thus, establishing a truncation tolerance of $\epsilon_{svd} = 10^{-6}$ would result, according to 12, in the use of 3 modes for ϕ_s , with none of them containing information that captures the relevant fluctuations in the anode, which are essential for the accurate representation of the FOM solution.

Furthermore, the electrochemical p2D model is characterised by the strong dependence of its dynamics on the non-linear function $j_{Li} = f_{j_{Li}}(\phi_s, \phi_e, c_s, c_e)$, which acts as either a source term or a boundary condition in all the system equations. Thus, the changes on the SVD truncation tolerance for a given variable will not necessarily correlate with the changes in the ROM solution error with respect to the FOM solution on that particular variable. Moreover, special attention must be paid to the fact that $j_{Li} \propto e^\eta$, with $\eta = \phi_s - \phi_e - U_{ocv}$, which implies that infinitesimal fluctuations in η may generate effects of a magnitude order of one in j_{Li} . Therefore, ϕ_s and ϕ_e have to be approximated with greater precision than j_{Li} to achieve a desired error in the reconstruction of the latter variable.

Concerning the proposed FOM, as mentioned above, we use a pseudo-spectral method (based on Galerkin projection) with N_r^* even order Legendre polynomials to solve c_s along the radial coordinate r^* . Hence, as previously introduced in Eq. 10b, results for this variable are given in the form of space and time distributions of Legendre polynomial coefficients $a_i^{r^*}(x, t)$ with $i = 1, \dots, N_r^*$, which can then be used to obtain the c_s distributions along r^* for any given value of x and t . The constant term associated to the zero order Legendre polynomial $a_0^{r^*}$ represents the average c_s value, while higher order terms are used to represent fluctuations along r^* . In the proposed ROM, the POD-modes used to represent the space distributions of $a_i^{r^*}$ coefficients are obtained using a *combined* modes strategy, where a single SVD is computed on a matrix formed by snapshots of all N_r^* coefficient distributions concatenated. In this case, it must be taken into account that the decrease of the associated singular values will be mainly driven by the $a_0^{r^*}$ component of the snapshots due to its higher characteristic value. Although this *combined* modes strategy presents the mentioned feature and requires careful analysis, it has been chosen over an *independent* modes approach to reduce the overall computational cost and avoid the fast-increasing number of DOFs in the ROM, since the latter strategy would require the computation of N_r^* SVDs and each Legendre polynomial coefficient $a_i^{r^*}$ would be represented by its own set of modes and time-dependant amplitudes to solve.

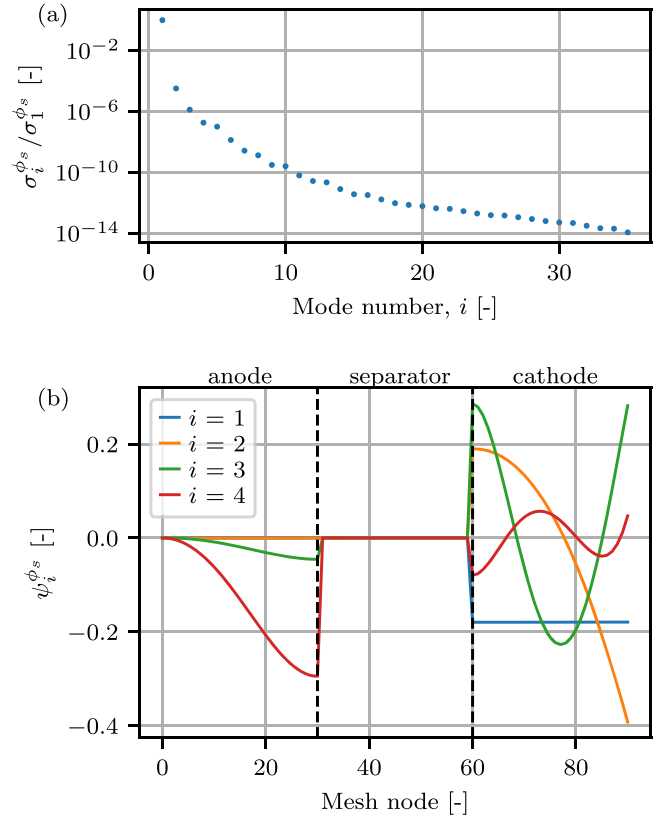


Figure 2. (a) Relative singular values of ϕ_s modes with respect to the first one, $\sigma_1^{\phi_s}$. (b) First four mode shapes of ϕ_s .

Moreover, note that the lithium exchange current at the surface of the active particles, j_{Li} , defined in Table I, shows the most complex distributions along the x dimension, and therefore, requires a higher number of modes than the other system variables in order to reconstruct it with sufficient precision. Hence, considering that the proper verification of the boundary conditions of the equation of mass conservation in the solid phase along x requires an accurate calculation of high order Legendre polynomial coefficients, the number of modes containing relevant information on the r^{*2} term in c_s has to be similar to the one required for j_{Li} in order for the ROM to work correctly, necessarily leading to the definition of a more restrictive SVD truncation tolerance for c_s .

Taking into account all this information, a truncation criterion to consider the relevant fluctuations in the dynamics is proposed,

$$n_2 = \min_{2 \leq i \leq N} \left\{ i \mid \frac{\sigma_i}{\sigma_2} < \epsilon_{svd} \right\}. \quad [13]$$

Similarly to 12, the criterion 13 also sets relative singular values but with respect to the second one, σ_2 . Figure 3 shows the relative singular values of all the system variables, computed following the above described criterion for a truncation tolerance of $\epsilon_{svd} = 10^{-6}$. The ones corresponding to variables ϕ_s , ϕ_e and c_e show a faster decay due to the already mentioned characteristic of their solution along the cell, while the more complex distributions of c_s and j_{Li} result into a significantly greater number of modes for the given truncation tolerance.

The fact that the truncation criterion used to select the number of modes to build the ROM 13 computes relative singular values with respect to σ_2 might cause discrepancies between the defined truncation tolerance ϵ_{svd} and the relative error of the ROM solution with respect to the FOM solution. Therefore, it is convenient to study how much can this number of modes be reduced while

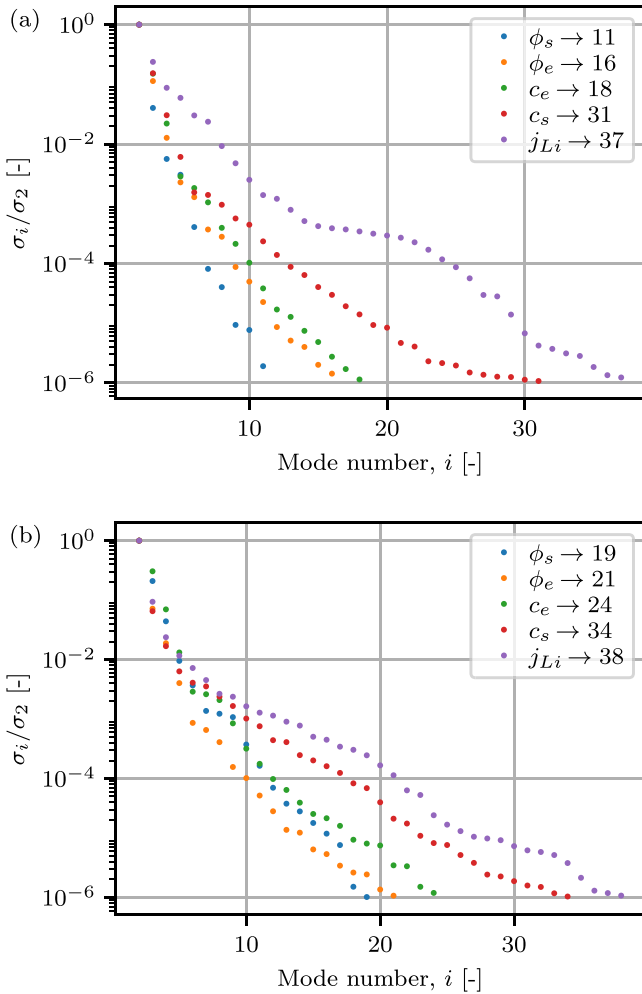


Figure 3. Relative singular values with respect to the second singular value, σ_2 of all p2D variables extracted from the (a) G-NMC and (b) G-LFP 0.5C full cell discharge snapshot matrices. The values showed in both legends correspond to the number of modes retained, n_2 , for an SVD truncation tolerance of $\epsilon_{svd} = 10^{-6}$ according to criterion 13.

maintaining the ROM relative error with respect to the FOM solution under a given threshold, ϵ_{err} . A detailed study of the case can be conducted using several pre-processed models, starting from the one proposed by the ϵ_{svd} criterion and gradually reducing the number of modes in every variable and non-linearity until a given maximum relative error threshold, ϵ_{err} , is reached. Table II shows the number of modes selected, n_{err} , following this procedure for $\epsilon_{err} = 10^{-3}$, under several C-rates and for two different cells, G-NMC and G-LFP. As it can be seen, the minimum number of modes n_{err} associated to each problem variable corresponds to a different SVD truncation tolerance ϵ_{svd} . Consequently, obtaining a good approximation of the solution below an established error threshold requires considering a different number of modes, n_{err} , to describe each variable, which turns out to be weakly dependent on the C-rate and the selected chemistry. Therefore, the main conclusion that can be drawn from this analysis is that the truncation criterion 13 is capable of retaining small fluctuations, which may be relevant to obtain accurate results, although determining the optimal number of modes requires the definition of different SVD truncation tolerances for each variable.

Some remarks concerning the selection of modes for the exchange current j_{Li} .—In addition to the guidelines on mode selection provided in the previous section, some care must be taken concerning the use of mixed finite element techniques in the FOM

and its effect on the derived ROM, taking into account that these schemes are known to produce numerical instabilities in some cases (see Ref. 21). In this particular case, such formulation results from the introduction of j_{Li} as an additional variable in the model, which is, as previously observed, quite convenient. Furthermore, in some cases a Lagrange multiplier could be introduced in the FOM in order to provide a reference for the electric potential, imposing a zero mean value for the electrolyte electric potential. The use of a mixed finite element formulation and the mentioned Lagrange multiplier lead, in both cases, to saddle point systems where well-posedness is not directly inherited by the discretised problem and can be a source of numerical difficulties in the ROM.

Considering the variety of ways in which a potential reference can be set in the FOM, it would be advisable to derive a ROM that is not affected by the particular choice made in the FOM implementation. If, for instance, the potential reference is imposed assigning a zero value to the electric potential in the electronic phase ϕ_s at one collector, the corresponding modes will inherit this property (since modes are extracted as linear combinations of observed fields) and there is no need to impose any additional condition in the ROM. It would be convenient to assume as well that the modes themselves provide a reference for the electric potential, avoiding any additional equation, when the reference is imposed through a Lagrange multiplier in the FOM to have a zero mean value for ϕ_e . It must be observed that the Lagrange multiplier in the FOM will correct the approximation of the exchange current j_{Li} in order to enforce the discrete version of the solvability condition

$$\int_0^{L_a} j_{Li} dx + \int_{L-L_c}^L j_{Li} dx = 0.$$

In the absence of this Lagrange multiplier in the ROM (under the proposed approach, where no additional equation will be added in the ROM in order to impose a reference for the electric potential, independently of the particular technique used in the FOM to impose it) the solvability of the electric potential in the derived ROM is not automatically guaranteed. In practice, however, usually this is not a problem provided similar quadrature formula are used in FOM and ROM. Nevertheless (see below) the correction in j_{Li} could have a relevant effect.

Lets consider now the approximation of j_{Li} in the mixed finite element formulation. It is well known (see Ref. 21) that numerical instabilities can arise in this kind of approximations if selection of finite element spaces do not satisfy a particular condition (known as inf-sup or LBB condition) related to the invertibility of the discretised operator. The violation of this condition leads to the presence of spurious components in the solution. In practice, the mixed finite element solution of the DFN model using P1 elements does not lead to such kind of instability. In contrast, the derived ROM could exhibit some numerical instability associated to the (almost) singularity of the discretised operator. Unsurprisingly, the selection of modes for j_{Li} and numerical quadrature schemes can have a strong effect on this behavior. These aspects are shortly considered below.

It must be taken into account that modes for the exchange current j_{Li} can be obtained from two sources: the variable j_{Li} in the (mixed finite element) FOM itself and the evaluation of the Butler-Volmer kinetics expression at the interpolation nodes using the remaining variable fields, leading to a second vector $f_{j_{Li}}$. Regarding the solution of Eq. 5, the error between vectors j_{Li} and $f_{j_{Li}}$ has two components, which are associated to:

- The value of the residual of the equation after the non-linear system has been solved.
- The difference in the numerical integration schemes of the terms associated to j_{Li} and $f_{j_{Li}}$.

The variable j_{Li} in the FOM is decomposed as a linear combination of FEM piecewise-linear basis functions, being the weights of that

Table II. Minimum number of modes n_{err} and associated SVD tolerance ϵ_{svd} for a pre-processed ROM simulation of the G-NMC and G-LFP cells at the indicated rates of charge (negative) and discharge (positive), obtained imposing a maximum relative error threshold of $\epsilon_{err} = 10^{-3}$ with respect to a reference FOM solution.

		0.5C		1.5C		−0.5C		−1.5C	
		n_{err}	ϵ_{svd}	n_{err}	ϵ_{svd}	n_{err}	ϵ_{svd}	n_{err}	ϵ_{svd}
ϕ_s	G-NMC	4	$3.0894 \cdot 10^{-3}$	4	$2.6947 \cdot 10^{-3}$	4	$2.3874 \cdot 10^{-3}$	4	$2.6432 \cdot 10^{-3}$
	G-LFP	5	$4.1557 \cdot 10^{-3}$	5	$3.2891 \cdot 10^{-3}$	5	$3.5650 \cdot 10^{-3}$	4	$7.6066 \cdot 10^{-3}$
ϕ_e	G-NMC	5	$1.3682 \cdot 10^{-3}$	7	$9.5250 \cdot 10^{-4}$	5	$5.5267 \cdot 10^{-4}$	8	$1.4132 \cdot 10^{-4}$
	G-LFP	8	$1.9524 \cdot 10^{-4}$	8	$3.6867 \cdot 10^{-4}$	8	$1.6709 \cdot 10^{-4}$	8	$1.5894 \cdot 10^{-4}$
c_e	G-NMC	9	$1.1109 \cdot 10^{-4}$	9	$1.1417 \cdot 10^{-4}$	10	$1.6338 \cdot 10^{-4}$	11	$2.3153 \cdot 10^{-4}$
	G-LFP	11	$1.2239 \cdot 10^{-4}$	12	$9.7804 \cdot 10^{-5}$	10	$1.8977 \cdot 10^{-4}$	10	$2.1421 \cdot 10^{-4}$
c_s	G-NMC	10	$2.1014 \cdot 10^{-5}$	11	$4.5593 \cdot 10^{-5}$	12	$1.3800 \cdot 10^{-5}$	17	$3.9407 \cdot 10^{-5}$
	G-LFP	15	$2.6290 \cdot 10^{-5}$	14	$7.3666 \cdot 10^{-5}$	15	$2.6099 \cdot 10^{-5}$	13	$4.8276 \cdot 10^{-5}$
j_{Li}	G-NMC	25	$8.5175 \cdot 10^{-5}$	28	$5.8822 \cdot 10^{-5}$	26	$8.4710 \cdot 10^{-5}$	29	$6.1781 \cdot 10^{-5}$
	G-LFP	34	$3.8765 \cdot 10^{-6}$	40	$1.7321 \cdot 10^{-6}$	38	$4.7198 \cdot 10^{-6}$	41	$4.4376 \cdot 10^{-6}$

linear combination the nodal values of j_{Li} . If the same numerical integration scheme is used for the terms associated to j_{Li} and $f_{j_{Li}}$, and the latter non-linear term is approximated in the same exact way as j_{Li} (i.e., as a linear combination of FEM piecewise-linear basis functions where each weight corresponds to nodal values of the non-linear function), the error between the two sets of nodal values can only be attributed to (a), which will generally be small compared to the characteristic value of j_{Li} . However, if a different numerical integration scheme is used to compute the terms associated to $f_{j_{Li}}$ and/or this non-linear term is not approximated in the same way as j_{Li} , part of the error between the two sets of nodal values is then a consequence of (b). In fact, this error may significantly increase when the case that is being solved has a strong non-linear behavior in the variable j_{Li} . This occurs when the gradients of the variables of the problem are high, what is typically caused by a strong demand of the cell electrical current, a highly unbalanced cell in terms of electrode capacities (which can result in higher exchange current gradients on the electrode with the smaller capacity for a given applied current), or very non-linear distributions of electrochemical properties along the cell.

Once that it has been established that differences between the nodal values of the j_{Li} variable returned by the FOM and the reconstructed nodal values of $f_{j_{Li}}$ for the solution of the same system might be significant, the question of what impact do these differences have on the solution of the ROM arises. The proposed p2D ROM considers that both j_{Li} and $f_{j_{Li}}$, as well as the rest of variables of the problem, are piecewise-linear functions. The use of the DEIM technique to reduce the computational cost associated to the evaluation of $f_{j_{Li}}$ term implies the definition of a set of modes used to describe it. As a result, the discrete block operator $B_{j_{Li}}^{j_{Li}}$ (see Appendix A for detailed description) introduced in Eq. 11e, resulting from linearisation in the ROM and associated to discretisation of Butler-Volmer kinetics and exchange current components, will depend on the selection of the mode source as well as on the details of the DEIM technique. Significant variations of the $B_{j_{Li}}^{j_{Li}}$ matrix conditioning can arise depending on the selection of the mode source used to represent the variable j_{Li} and the non-linear field $f_{j_{Li}}$ in the ROM: left singular vectors from the matrix $\Psi_{j_{Li}}$ or from the matrix $\Psi_{f_{j_{Li}}}$. This is observed when the manifolds associated to two different sets of modes begin ceasing to be close, which seems to occur approximately for the mode \hat{i} , when

$$\sigma_{\hat{i}} \sim \frac{\|X_{j_{Li}} - X_{f_{j_{Li}}}\|_2}{\sqrt{n_s}}, \quad [14]$$

where $X_{j_{Li}}$ and $X_{f_{j_{Li}}}$ are the snapshots matrices of j_{Li} and $f_{j_{Li}}$, respectively, and n_s is the total number of mesh nodes corresponding to the subdomains where these fields are defined.

Figure 4a shows the evolution of singular values for both j_{Li} and $f_{j_{Li}}$ for the baseline case, where the estimate of $\sigma_{\hat{i}}$ points out that the divergence in mode shapes approximately starts at $\hat{i} = 24$. Figure 4b, on the other hand, illustrates how the conditioning of the ROM matrix $B_{j_{Li}}^{j_{Li}}$, steeply increases when the number of modes used is greater than \hat{i} for the case in which different sets of modes are used to represent the variable j_{Li} and the non-linear field $f_{j_{Li}}$ in the ROM. Note also that if the same set of modes is used to describe both terms, the conditioning of the $B_{j_{Li}}^{j_{Li}}$ matrix remains low and stable for any given number of modes and the ROM will converge to a solution. Nevertheless, the use of the $\Psi_{j_{Li}}$ modes results in a solution of lower quality, since these modes (in the case that is being discussed) are obtained from the solution of the system using a higher order numerical scheme to integrate the non-linear term $f_{j_{Li}}$. In the ROM, this last term, as well as its derivatives with respect to the rest of the variables, are evaluated at the DEIM points (which are mesh nodes) and integrated using exact schemes after assuming that $f_{j_{Li}}$ is piecewise-linear. Therefore, the modes $\Psi_{j_{Li}}$ reconstruct the $\hat{\beta}_{j_{Li}}^h$ vector with less accuracy than the $\Psi_{f_{j_{Li}}}$ modes.

The possibly existing differences in the regularisation of the non-linear term $f_{j_{Li}}$ between the FOM and the ROM also account for the worse behavior of the model when the $\Psi_{j_{Li}}$ modes are used. Consequently, the use of the $\Psi_{f_{j_{Li}}}$ modes to describe both j_{Li} and $f_{j_{Li}}$ constitutes the most robust approach to solving the ROM, although the quasi-singularity of the ROM discrete linearised operator cannot be completely ruled out and spurious components could in principle arise during the ROM time-integration. A general technique to ensure the numerical stability of ROMs derived from mixed finite element approximations of the DFN model would be highly appreciated.

Error estimators.—As previously explained, the assessment of the ROM accuracy is a key ingredient in time-adaptive ROMs. A first approach, proposed in Ref. 17, consists in the use of local residuals. In particular, FEM residuals are being considered here in order to obtain a measure of the error made by the ROM. The system formed by Eqs. 1–5, which constitutes the variational form of the DFN model, leads after time-discretisation to a problem that can be written with the general form

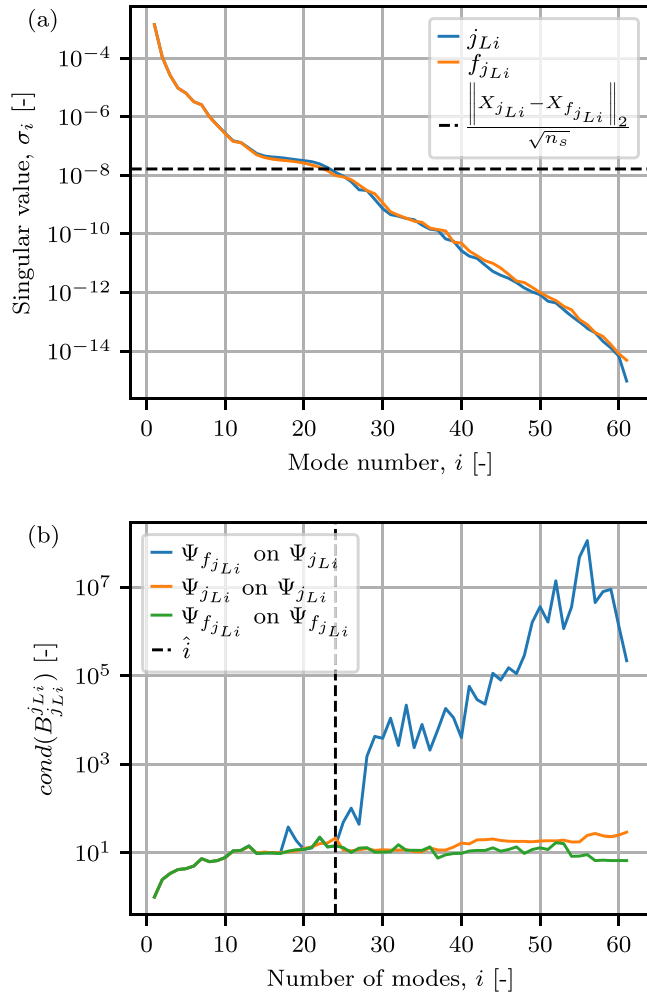


Figure 4. (a) Singular values evolution of j_{Li} and $f_{j_{Li}}$. (b) Conditioning number of the ROM matrix $B_{j_{Li}}^{j_{Li}}$ as a function of the number of modes used for different combinations of the modes used to describe the variable j_{Li} and the non-linearity $f_{j_{Li}}$. Building such matrices involves, in each case, projecting one set of modes onto the other.

$$\text{Find } \mathbf{u} \in V \text{ such that} \\ B(\mathbf{u}, \mathbf{v}) + N(\mathbf{u}, \mathbf{v}) = L(\mathbf{v}) \quad \forall \mathbf{v} \in V, \quad [15]$$

where \mathbf{u} and \mathbf{v} are the solution and test function vectors in the vector space V , respectively, and $B(\cdot, \cdot)$, $N(\cdot, \cdot)$ and $L(\cdot)$ are bilinear, non-linear and linear forms (defined either on the vector space V or on $V \times V$), respectively. A residual vector of the system for a given approximation to the solution $\hat{\mathbf{u}} \in V$ can then be assembled using

$$\mathbf{r}_{\hat{\mathbf{u}}, \mathbf{v}} = L(\mathbf{v}) - B(\hat{\mathbf{u}}, \mathbf{v}) - N(\hat{\mathbf{u}}, \mathbf{v}) \quad [16]$$

with \mathbf{v} stepping through a suitable collection of functions \hat{V} . The computation of the system residuals for a given solution is explicit and only requires choosing the set $\hat{V} \subset V$ of test functions. It should be remarked that the implemented ROM (based on the Galerkin method, consisting in replacing V by \hat{V}_h with $\hat{V}_h \subset V_h \subset V$ in 15) would make residuals defined by 16 virtually zero if \mathbf{v} is taken in \hat{V}_h . Residuals corresponding to functions \mathbf{v} outside \hat{V}_h instead will provide information on the accuracy of $\hat{\mathbf{u}}$.

In the case of the proposed ROM, an alternative to build \hat{V} could be the gathering of a set of Lagrange basis functions associated to a selection of interpolation nodes in the finite element discretisation. This proposal seems suitable since the numerical integration of the

resulting expression is computationally inexpensive (still having $\hat{V} \subset V$) and clearly provides local information.

However, the highly non-linear coupling between partial differential equations, the presence of a subscale associated to the particle radius and the multi-region nature of the problem prevent the correlation of local errors with residuals, as it is done in Ref. 17 through a calibration process for a single scalar partial differential equation. Moreover, the residual values can overestimate the error made by the model at those mesh nodes where natural boundary conditions have been imposed in the weak form of the system. Figure 5 depicts this behavior comparing, for the 0.5C discharge of the G-NMC cell, the relative error between the ϕ_s solution of a pre-processed ROM and the analogous FOM with the relative FEM residual of the ϕ_s equation computed using the ROM solution. The pre-processed ROM, in this case, has been built only with the initial 5% snapshots of the FOM solution in order to emulate the behavior of the initial ROM stage of a time-adaptive ROM strategy (which is described in detail below). For the results shown in Fig. 5a, residuals have been computed with \mathbf{v} stepping through the whole FOM function space, thus having $\hat{V} = V_h$ and being able to represent the resulting residual vector as a nodal distribution for the corresponding solution at the given time. On the other hand, Fig. 5b represents the evolution in time of a single residual value, computed with \hat{V} only being the basis function of the FOM function space V_h corresponding to the given mesh node. The vertical red dotted lines in Figs. 5a and 5b indicate the mesh node and time step for which the time and space distributions are given, respectively. The space distributions at approximately half of the discharge cycle clearly show how the FEM residual does not accurately represent the drop in the error at the anode current collector due to the fact that it does not have any information on how both ROM and FOM impose the same reference ϕ_s value at this node. Additionally, the residual space distribution shows a much more oscillatory behavior than the one of the actual error, with peak minimum values that represent drops of a couple orders of magnitude with respect to their mean value (particularly in the cathode of the cell). Regarding the time distribution for a node at the centre of the anode, there is some coherence between the residual and error evolution, with a slight increase in the gap between them as the simulated time increases and, again, a more oscillatory behavior of the residual curve.

Thus, although these FEM residuals provide some qualitative information concerning ROM errors, they cannot be calibrated in order to be used as an error estimator to be included in an automatic ROM-adaption device. In addition, given the selection of \hat{V} specified above, the computed residuals provide information related to the error with respect to the FOM solution and not to the true solution of the DFN model which, in combination with an estimation of the approximation error of the FOM, could be very useful to establish automatic criteria on the error estimator thresholds of the time-adaptive ROM. In order to overcome these difficulties, it is convenient to compute directly error estimators for each one of the variables of the problem. To this end, implicit *a posteriori* error estimators of the FEM²² for the DFN model can be implemented which, as it will be shown, are precisely based on the computation of some residuals. To obtain these estimators, a linearisation of the problem 15 must be derived. Let such linear problem, in variational form, be written as

$$\text{Find } \mathbf{u}_e \in V \text{ such that} \\ \hat{B}(\mathbf{u}_e, \mathbf{v}) = \hat{L}(\mathbf{v}) \quad \forall \mathbf{v} \in V, \quad [17]$$

where \mathbf{u}_e is the exact solution of the linearised problem. The error associated to $\hat{\mathbf{u}}$, defined as $\mathbf{e} = \mathbf{u}_e - \hat{\mathbf{u}}$, thus verifies

$$\begin{aligned} \hat{B}(\mathbf{e}, \mathbf{v}) &= \hat{B}(\mathbf{u}_e, \mathbf{v}) - \hat{B}(\hat{\mathbf{u}}, \mathbf{v}) \\ &= \hat{L}(\mathbf{v}) - \hat{B}(\hat{\mathbf{u}}, \mathbf{v}), \end{aligned} \quad [18]$$

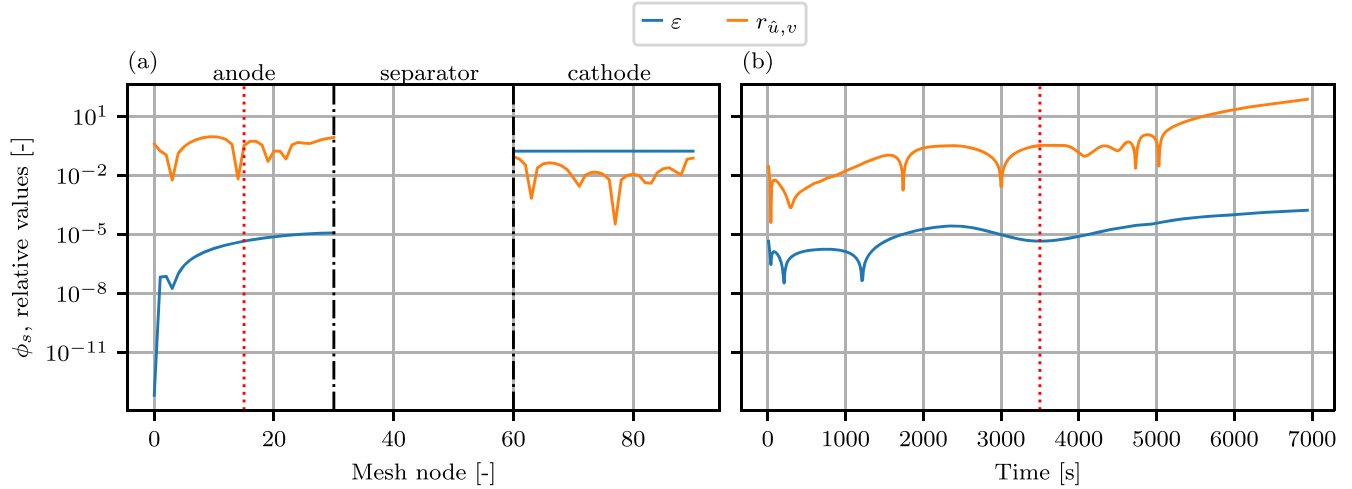


Figure 5. ϕ_s error (with respect to reference FOM solution) vs ϕ_s equation FEM residual of the solution of a pre-processed ROM built with the initial 5% snapshots of the FOM solution. Distributions along the cell thickness for time $t = 3500$ s (a) and along time for mesh node $n_i = 15$ (b).

which defines the linear problem to be solved in order to compute \mathbf{e} . In this particular case, in order to obtain a linear system of general form 17 from the non-linear system 15, a first order Taylor series at the obtained solution $\hat{\mathbf{u}}$ is used for all the system non-linearities. It must be remarked that this linearisation results in the right hand side or *source term* of the error system 18 matching the residual of the system for that solution, $\mathbf{r}_{\hat{\mathbf{u}},v}$, and the first order derivatives of the non-linearities with respect to the variables of the problem being included in the bilinear form associated to the error vector, $\hat{B}(\mathbf{e}, \mathbf{v})$.

The error system 18 can be solved globally (at the whole cell domain) or locally (at a previously selected number of elements). The first option has a computational cost of the same order of magnitude as the one of solving the FOM for each time step, although smaller since the resulting problem is linear and Newton (or the selected numerical scheme) iterations are not needed. The latter option is optimal for the ROM implementation due to its low computational cost, especially when compared to the first option. However, solving the error system locally requires the definition of additional natural (Neumann) boundary conditions at those element boundaries that do not intersect with any exterior or interior subdomain boundaries of the cell domain. This problem is solved by approximating the flux at the boundaries of each selected element K using the solution for which the error is being estimated at K and its neighbouring elements J ,

$$\frac{\partial \mathbf{u}}{\partial \mathbf{n}_{K \cap J}} \approx \frac{1}{2} \mathbf{n}_{K \cap J} \cdot \{(\nabla \hat{\mathbf{u}})_K + (\nabla \hat{\mathbf{u}})_J\}, \quad [19]$$

thus introducing a relevant source of uncertainty. To address this issue, the ratio between the solutions of the global error system and the local error system at a given K element for the initial time step, $\mathbf{e}_0|_K$ and $e_{K,0}$, respectively, can be computed and used as a correction factor for local error estimators,

$$f_{e_{K,0}} = \frac{\mathbf{e}_0|_K}{e_{K,0}}.$$

Figure 6 shows how, for a given mesh element in the centre of the anode ($K = 15$), the agreement between both global and local (corrected) error estimators and the actual error between the ROM and the reference FOM solution for the case introduced earlier in this Section is much better than the one of the equation residuals, both in terms of order of magnitude and evolution in time. It can also be seen that, as expected, the global error estimator gives a better approximation of the actual error than local error estimator and both of them become less accurate as the model is further integrated in time.

Once the suitability of local error estimators for the role of time-adaptive ROM error estimators has been determined, the dependency of the values and evolution of the final error estimator of each variable on the chosen set of elements K can be mitigated by introducing a new correction factor that directly relates them to a single global measure of the global error estimator at the initial ROM simulation time

$$f_{\hat{\mathbf{e}}_{K,0}} = \frac{\|\mathbf{e}_0\|_2}{e_{K,0} \sqrt{n}},$$

with n being the number of mesh nodes in which the error is defined. Note that this correction might lose its validity as the ROM integrates further in time and has to be updated at every ROM adaption stage of the time-adaptive algorithm. All the N_K corrected local error estimators can be averaged, having the final expression for the error estimator $\hat{\mathbf{e}}$ of any given variable of the time-adaptive ROM strategy

$$\hat{\mathbf{e}} = \frac{1}{N_K} \sum_{i=1}^{N_K} e_{K_i} f_{\hat{\mathbf{e}}_{K_i,0}}. \quad [20]$$

Concerning the determination of the elements in which the local error estimators are computed, three different approaches have been considered:

- The use of elements associated to DEIM points, used by the ROM to compute all the non-linearities of the system (and their derivatives) and interpolate them at the rest of the cell domain.
- The use of points derived from performing the DEIM technique on snapshots of ROM residuals computed on the whole domain.
- The determination of the elements through the previous study of relative error maps between a pre-processed ROM solution and a reference FOM solution.

The location of the DEIM points along the cell domain provides very useful information about the complexity of the system solution and thus, it can be assumed that it also provides relevant information on the optimal positioning of the local error estimator probes. The advantage of using these points for such purpose is that it does not require any additional calculations. In order to justify the validity of this approach, Fig. 7 shows the position of the first 20 DEIM points obtained from the relative error maps that result of comparing the solution of a pre-processed ROM with a reference FOM solution for each system equation, consequently labeled. It also includes the

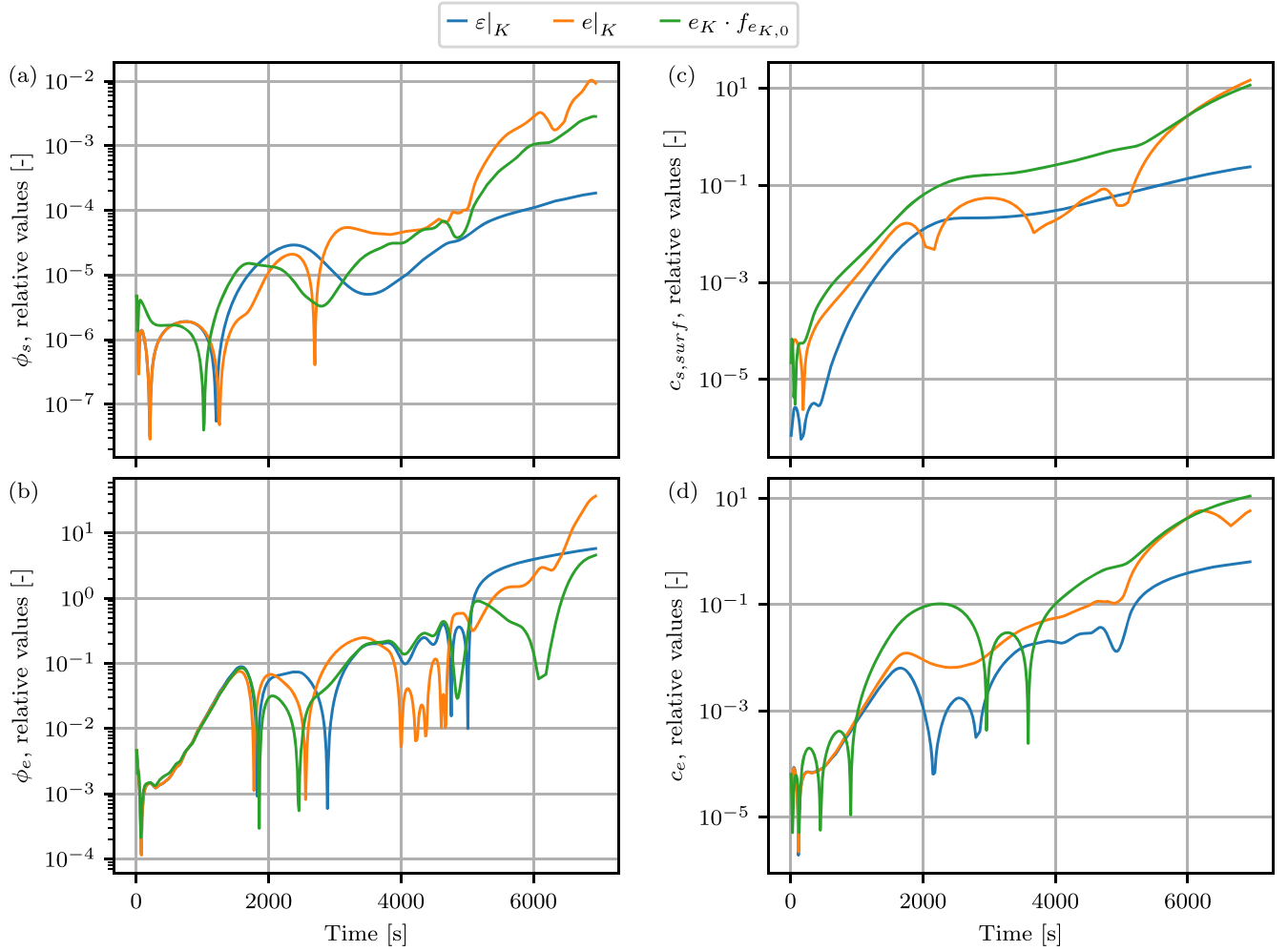


Figure 6. Error (with respect to reference FOM solution), global and corrected local error estimators evolution in time of the solution of a pre-processed ROM built with the initial 5% snapshots of the FOM solution. Electric potential in the solid (a) and electrolyte (b) phase, and lithium concentration at the surface of the active particles (c) and in the electrolyte (d) at mesh element $K = 15$.

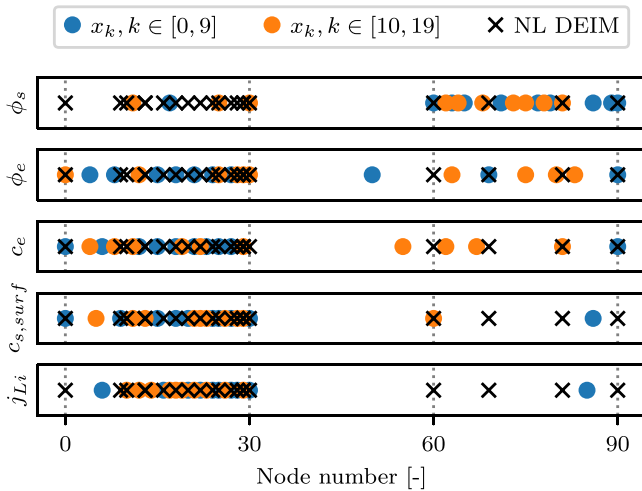


Figure 7. Location of the first 20 *DEIM points* of relative error fields vs non-linearities of the system.

position of the DEIM points used by the pre-processed ROM to interpolate the non-linearities (NL) of the problem. In both cases, these points are mainly located near the current collectors and the subdomain boundaries, denoted by vertical dotted lines in the figure.

The fact that most of the points concentrate in the anode of the cell (from nodes 0 to 30) is directly related to the difference in morphology and electrochemical properties between the electrodes for the selected cell, which results in significantly stronger gradients in the anode for most variables. The proximity of the points to current collectors and subdomain interfaces is directly related to the imposition of natural boundary conditions on the weak form of the problem. Regarding ϕ_s , the much higher effective electronic conductivity in the anode with respect to the cathode results in more constant distributions in the first electrode, which imply that the model will present larger relative errors in the cathode. This particular behavior in the error maps is not very well identified by the position of the NL DEIM points.

Therefore, it can be concluded that the DEIM points computed for the interpolation of the non-linearities give a good approximation to the optimal positioning of ROM error estimator probes, as long as it is ensured that both electrodes are sufficiently represented. Moreover, the obtained results show how the number of probes used to estimate the overall ROM error can be reduced with respect to the number of non-linearity DEIM points by simply hand-picking a distribution of points that ensures that domain boundaries and subdomain interfaces, as well as some interior points in both electrodes, are represented.

Time-adaption strategy.—The strategy designed for the p2D time-adaptive ROM following some ideas from Ref. 17 is illustrated in Fig. 8, essentially consisting in the combination of:

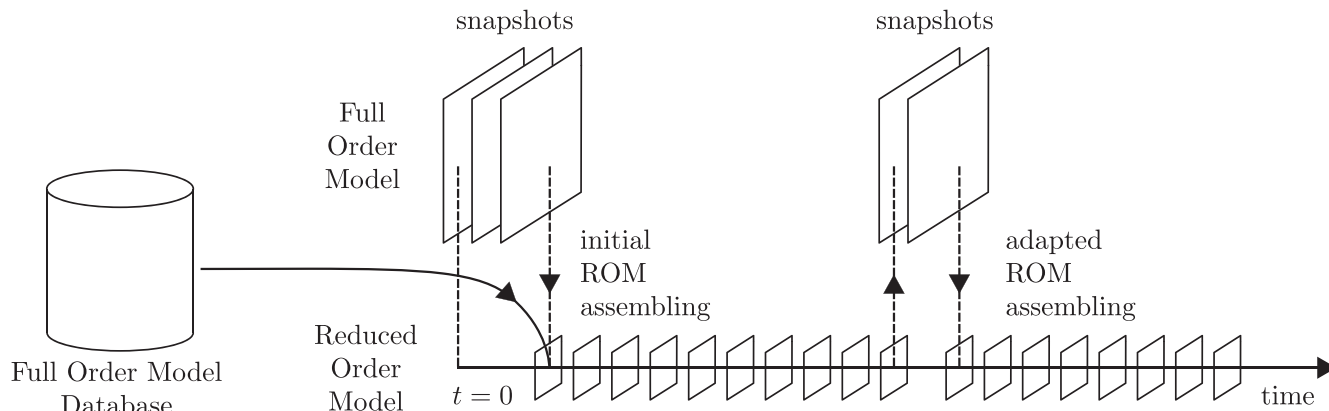


Figure 8. Time-adaptive ROM strategy.

- The initialisation of the simulation using the FOM, which provides the first set of modes used to assemble the initial ROM. These modes will be used to perform an initial adaption of the database-build modes, if present, to better represent the actual cell that is being simulated.

- The alternation of calls to the ROM and very brief calls to the FOM during the time integration of the model. The latter are produced when the ROM solution loses its accuracy, providing enough information to include in the ROM and restoring the quality of the ROM-solution.

As previously introduced, this strategy does not require a database of FOM simulations. In fact, this is the main advantage of the adaptive ROM proposed here. Nevertheless, in some cases some information from the FOM may be available. This would be the case during cell optimisation, since other cells would have been simulated during previous optimisation iterates. Information from these solutions (sharing the same cell chemistry but with different design parameters and probably also subject to different applied currents), if available, can also be used in the derivation of the initial ROM (as shown in Fig. 8).

The evaluation of the accuracy of the ROM solution with respect to the FOM requires the definition of one or more error estimators. A strategy based on the definition of control parameters, such as error estimator tolerances for each problem variable, relative tolerances used to truncate the number of modes used for each variable as well as mode-adaption parameters, has been developed to allow the automated yet safe time integration of the adaptive model. These control parameters are:

- Fraction of the (estimated) total simulation time that the initial FOM will solve, $\chi_{t,0}^{fom}$.
- Fraction of the initial FOM simulation time that the subsequent calls to the FOM during the simulation will solve, $\chi_{t,0}^{fom}$.
- Fraction of the (estimated) total simulation time that the initial ROM will solve, $\chi_{t,0}^{rom}$.
- Maximum fraction of the (estimated) total simulation time that any call to the ROM during the simulation will be allowed to solve, χ_t^{rom} .
- Relative tolerance value for the ROM error estimator, $\epsilon_{\hat{\epsilon}}$. When exceeded, the model will automatically return to the use of the FOM for the prescribed number of iterations.
- Relative truncation tolerance for the SVDs performed in all ROM assemblies, ϵ_{svd} .
- Fraction of the database (if used), filtered by suitability to the simulated case, used during the initial ROM assembly, χ_{db} .

Finally, in order for the time-adaptive ROM to work, an adaptation criteria needs to be defined. As introduced previously, the modes used to construct the reduced model are adapted after

each FOM time-integration stage in order to maintain a proper solution accuracy. The algorithm proposed in Ref. 17 is used to update the modes basis. It consists in the application of POD to a set of weighted vectors that combines the old modes, used in the previous ROM time-integration stage, with the new modes extracted from applying POD to the snapshots of the last FOM time-integration stage. The weights used to combine the different vectors are conveniently computed in order to eliminate the modes that are not being used to represent the solution in the last ROM stage while not enhancing the modes whose amplitudes have increased excessively (which could destabilise the model).

Results

A methodology to build time-adaptive ROMs based on the DFN model has been proposed above. As already mentioned and for the sake of simplicity, the application of this methodology has been illustrated using a p2D model, although its extension to p4D models is straightforward. In this section, the proposed methodology will be applied to several cases in order to confirm its robustness. In particular, detailed results are discussed for a G-NMC cell under two loading conditions: the previously introduced baseline case, consisting on a 0.5C full discharge, and a hybrid load cycle. In addition, cell voltage curve results under several utilization conditions (charge and discharge at different C-rates) are shown for both G-NMC and G-LFP cells.

In the present section, the fraction of simulated time where the FOM is used within the time-adaptive strategy is presented as a measure of simulation acceleration. The key idea that justifies the use of this measure instead of actual simulation times is that the cost of integrating the ROM in time is negligible compared to the FOM if the reduction of DOFs solved by the first with respect to the latter is sufficient. Thus, the time-adaptive ROM strategy will ideally provide a computational cost reduction factor equal to the inverse of the fraction of the simulated time integrated by the FOM. In the case of the presented p2D examples, the FOM solves a domain discretised into 90 elements (30 per subdomain), resulting in a total of 430 DOFs. For this particular discretisation of the problem, which already results in a computationally inexpensive FOM, it can be assumed that the ideal speed-up factor will not be achieved by the time-adaptive strategy. However, the goal of these examples is not to evaluate the actual simulation time reduction, but to illustrate the accuracy and robustness of the proposed methodology through the analysis of their results and the use of the presented simulation acceleration measure. Additionally, results for a high-resolution p4D case (where the use of a large number of mesh elements is justified by the necessity to accurately represent three-dimensional effects) are shown and simulation times are provided, validating the use of the chosen simulation acceleration metrics on the p2D cases.

Appendix B contains all the data used to obtain the examples presented here. Cell parameters (both morphological and

Table III. Time adaptive strategy control parameters.

Parameter	Value
$\chi_{t,0}^{fom}$ [-]	0.05
$\chi_{t,0}^{rom}$ [-]	0.25
$\chi_{t,0}^{rom}$ [-]	0.95
χ_t^{rom} [-]	0.95
$\epsilon_{\hat{\epsilon}}$ [-]	10^{-2}
$\epsilon_{svd}(\phi_s)$ [-]	10^{-3}
$\epsilon_{svd}(\phi_e)$ [-]	10^{-4}
$\epsilon_{svd}(c_s)$ [-]	10^{-6}
$\epsilon_{svd}(c_e)$ [-]	10^{-4}
$\epsilon_{svd}(j_{Li})$ [-]	10^{-6}
$\epsilon_{svd}(\beta_{j_{Li}})$ [-]	10^{-6}
$\epsilon_{svd}(\beta_{c_e})$ [-]	10^{-5}

electrochemical) are given in Tables B-1 and B-2, while Table B-3 describes simulation parameters. The control parameters of the time-adaptive strategy (as defined previously) used for all the simulations corresponding to the results shown in this Section are presented in Table III. The error estimator $\hat{\epsilon}$ for each variable is computed as a simple moving average with a window of 10 time steps of the mean value of the corrected local error e_K computed at elements $K = \{0, 15, 29, 60, 75, 89\}$ and following expression 20.

Lets consider first the simulation of the G-NMC cell discharge at a 0.5 C-rate. Figure 9a shows the cell voltage (the main performance indicator at a macroscopic level) of the implemented time-adaptive model. As indicated in the legend of the figure, the curve components in blue correspond to time periods where the solution

is computed using the FOM and those in orange to time periods where the ROM is used instead. A reference solution, where the FOM is used to compute the solution during all the cell utilization period, is also represented as a black dashed curve in order to assess the accuracy of the time-adaptive ROM. As it can be seen, the result is in excellent agreement with the reference solution, obtained from the numerical simulation of the FOM. The number of DOFs used in the ROM after each update is specified in the plot, showing a very important reduction when compared to the FOM. Also, note that the number of time steps performed by the FOM represent a $\sim 10\%$ of the total simulated time, implying that an ideal speed-up factor of ~ 10 could be achieved in an analogous p4D simulation.

As expected given the conservative selection of parameters in the proposed methodology, the number of DOFs of the subsequent ROMs after each adaption stage increases. However, the time periods that the ROMs are able to integrate while maintaining the error estimator values below the preset threshold also increase as the number of DOFs increases, since the models have more information about the solution of the problem and the adapted modes can represent a larger range of the dynamics of the system. On the other hand, Fig. 9b illustrates the evolution of the error estimators of each variable in time, revealing how the solution deteriorates as the model is integrated in time further away from the initial condition imposed after each ROM adaption stage. Note how, generally, the rate at which the error estimators grow in value decreases after each adaption stage.

Figures 9c and 9d show the results of the application of this methodology to the simulation of the cell now subject to a hybrid cycle with C-rates of up to 2C (see Fig. B-2 of Appendix B). Although this represents a much more complex utilization case (involving completely different profiles for internal variables during charge and discharges phases, and considering relatively high currents), the performance of the time-adaptive ROM is quite similar

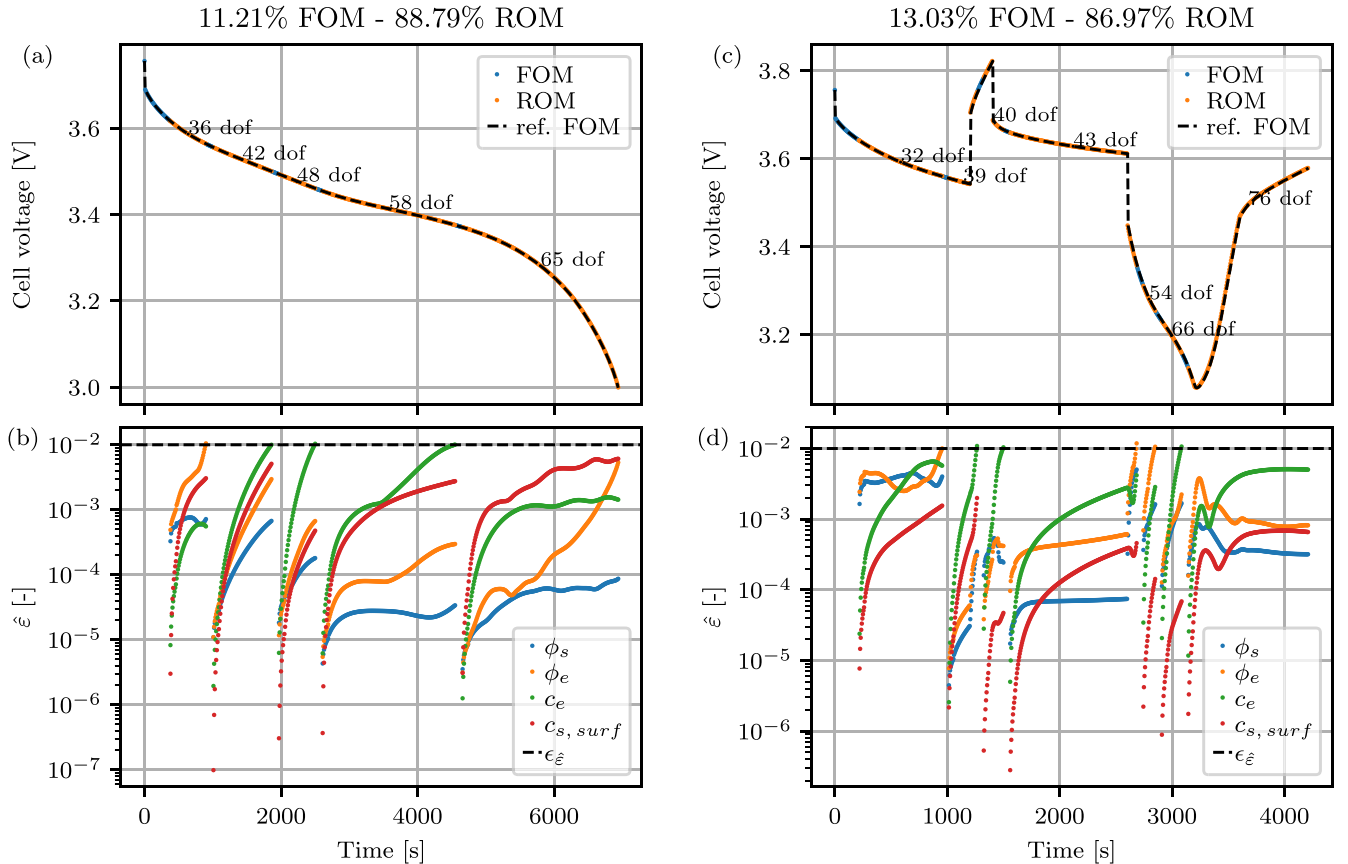


Figure 9. Voltage curve and ROM error estimator evolution corresponding to the simulation of the p2D time-adaptive ROM of a G-NMC cell for a constant 0.5 C-rate discharge, (a) and (b), and a hybrid cycle, (c) and (d).

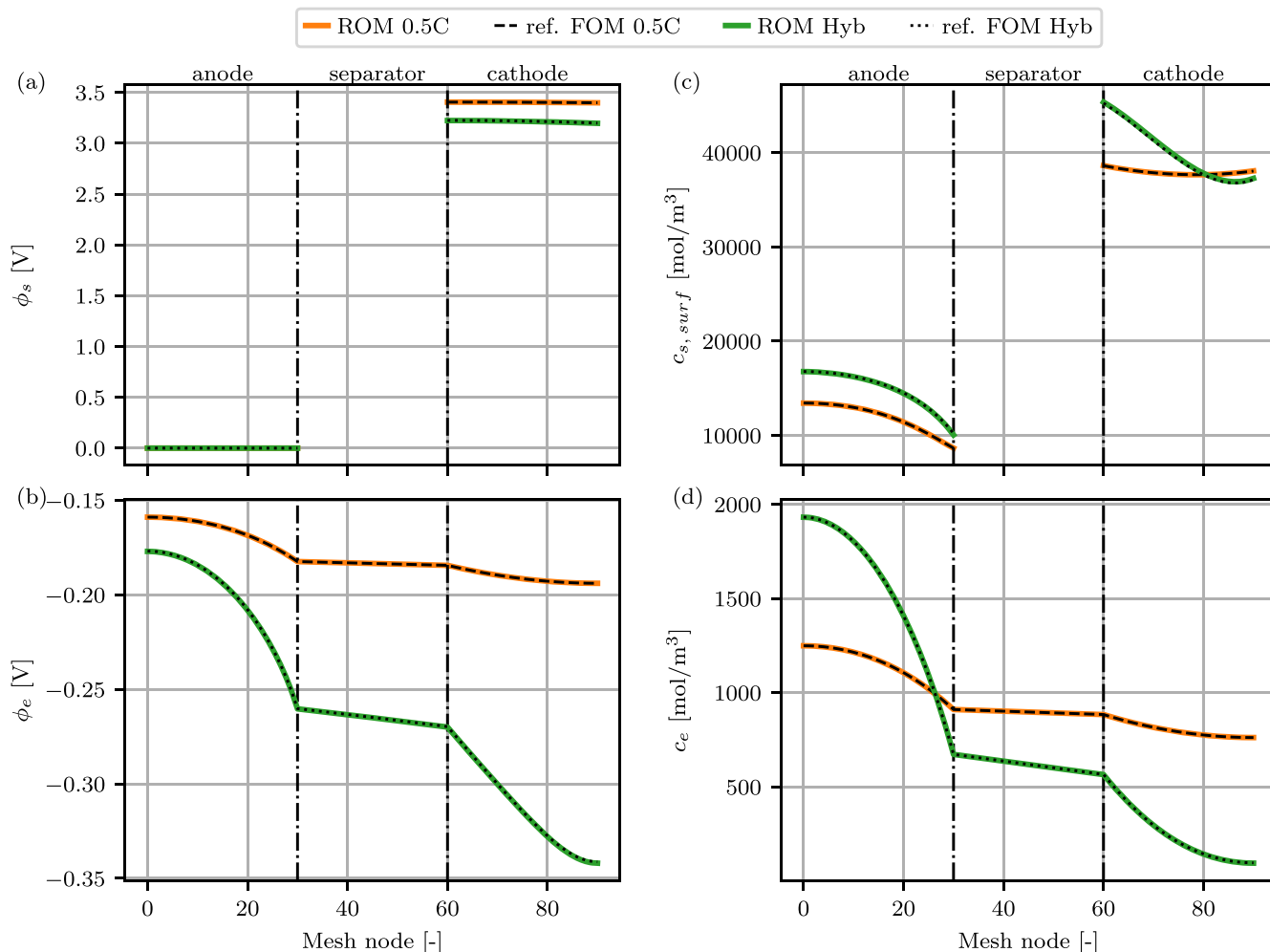


Figure 10. Distributions of variables of the problem along the cell thickness for the solution of the p2D time-adaptive ROM of a G-NMC cell under 0.5 C-rate discharge (see Figs. 9a and 9b) and hybrid load cycle (see Figs. 9c and 9d) conditions with respect to their corresponding FOM reference solutions at times $t = 4000$ s and $t = 3000$ s, respectively.

to the previous case. Agreement with the reference solution is again excellent and the total simulation time fraction where the FOM is used is only slightly higher than the one of the baseline case, with the number of DOFs of the ROM being even smaller during some time periods. Robustness of the proposed methodology is then remarkable, especially considering that the same selection of parameters is used in all the examples.

A closer look into the results provided by the time-adaptive ROM is now taken. So far, accuracy has been assessed only using the cell voltage. Now, prediction of internal variables is also considered. For the sake of brevity, only the G-NMC 0.5C discharge and hybrid loading cycle are presented. Figure 10 shows how the time-adaptive ROM solution provides distributions along the cell thickness of the different variables of the problem that accurately represent the reference FOM solution in both cases, even for times where some of the error estimators are about to reach the threshold value, manifesting the robustness of the chosen estimators and time-adaptive strategy control parameters.

Additionally, Fig. 11 shows how the lithium-ion exchange current density and concentration gradient in the electrolyte, which present more complex distributions along the cell thickness and typically require a larger number of modes than the rest of variables of the problem, are also represented with satisfactory precision. As it can be seen, the model successfully reproduces the more demanding profiles of the hybrid load cycle, where more complex dynamics have been excited and the corresponding distributions for the chosen time (where the applied current is 2C) present higher orders of

magnitude for these two fields with respect to the baseline 0.5C discharge case.

In order to complete the analysis of the proposed methodology, higher charge and discharge currents are considered. Since electrode utilization is more and more heterogeneous as the cell is subject to higher currents, these high current cases result in more challenging tests for the time-adaptive ROM. But, as shown here, the proposed time-adaptive ROM also proves to be efficient and accurate for higher charge and discharge rates across different cell chemistries and configurations. Figure 12 represents the voltage curves of the time-adaptive ROM and the reference FOM solution for C-rates of up to 5C for both G-NMC and G-LFP cells. Clearly, this figure depicts a very good agreement with the reference solution in all the considered cases.

Finally, results of the application of this methodology to the p4D case are shown. This is, as explained, the ultimate goal of this development. For that purpose, the open source p4D model *cideMOD*, presented in Ref. 23, has been used as the FOM within the time-adaptive strategy implementation, and also to generate the reference solution. Figure 13a shows the time-adaptive p4D ROM voltage curve for a 0.5C full discharge of a G-NMC cell, which directly corresponds to the p2D case presented earlier in Fig. 9a. Additionally, Table IV summarises model discretisation and performance information for the p4D case, including simulation times. It can be seen how the quality of the approximation with respect to the reference solution is comparable to the one provided by the time-adaptive p2D implementation, and so is the fraction of time

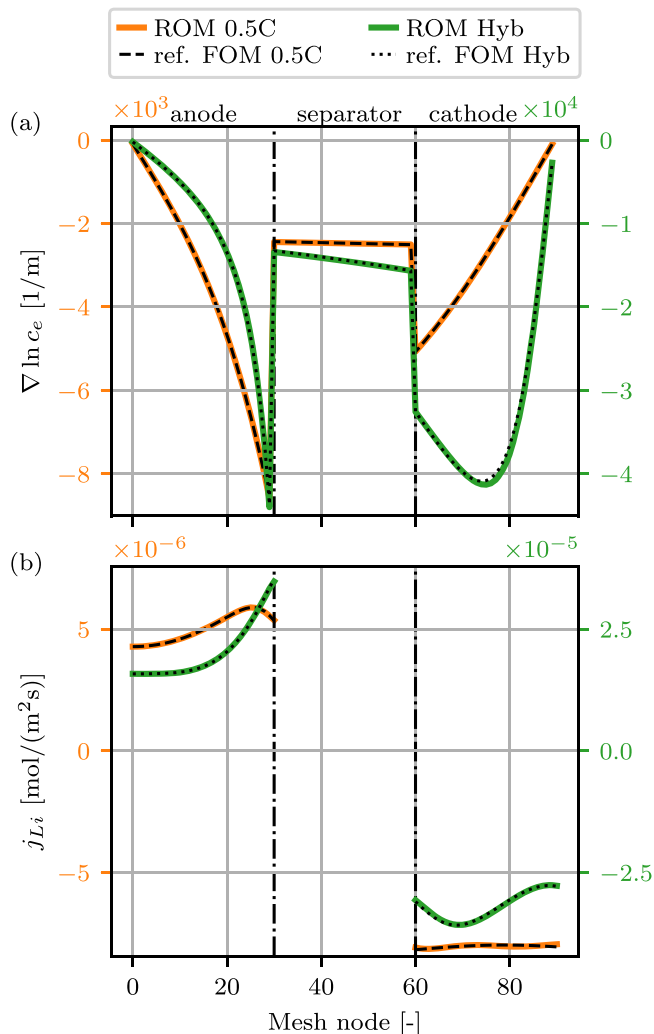


Figure 11. Distributions of lithium-ion exchange current density and concentration gradient in the electrolyte along the cell thickness for the solution of the p2D time-adaptive ROM of a G-NMC cell under 0.5 C-rate discharge (see Figs. 9a and 9b) and hybrid load cycle (see Figs. 9c and 9d) conditions with respect to their corresponding FOM reference solutions at times $t = 4000$ s and $t = 3000$ s, respectively.

simulated by the FOM using the same time-adaptive strategy control parameters. In this case, this fraction (10.47%) results in a simulation acceleration factor of 9.39 which is, as expected for a p4D case, remarkably close to the ideal acceleration factor of $1/0.1047 = 9.55$, hence justifying the use of the fraction of simulated time solved by the FOM as a measure of simulation acceleration in the analysis shown above. It can also be noted how the DOFs in the FOM (linked to the geometry description) increase by several orders of magnitude (see Fig. 13b for a 3D representation of the p4D case mesh), while the number of DOFs in the ROM (related instead to the solution dynamics) only increase slightly in comparison to the analogous p2D case.

Conclusions

An efficient and robust methodology has been developed for the construction of a time-adaptive ROM for the p2D electrochemical model obtained by Newman and co-workers in Ref. 5. The development of this more effective time-adaptive strategy is not straightforward because of the inherent intricacy of the electrochemical problem. Its complex behavior requires both a careful analysis to select the relevant modes that describe the dynamics of the system

Table IV. Time-adaptive p4D ROM and reference FOM comparison. Computational times have been obtained using the processor Intel® Core™ i9-10900 CPU @ 2.80 GHz × 20.

	Reference FOM	Time-adaptive ROM
Number of mesh elements		197967
Number of mesh nodes		36902
Number of DOFs	182167	{39, 46, 53, 62, 70}
Simulated time [FOM/ROM]	100%/0%	10.47%/89.53%
Simulation time [hours]	34.08	3.63

and the introduction of efficient error estimators, which are more involved than those used in adaptive models for simpler problems.

Regarding mode selection, our analysis deals with critical aspects of the p2D DFN model, characterised by a strong dependence of its dynamics on the non-linear function describing the Butler-Volmer kinetics. In particular, we establish a new truncation criterion to determine the number of modes required to account for small fluctuations in certain variables, such as ϕ_s and c_e , which turn out to be very important for accurately representing the FOM solution. Another key aspect of the problem, which may dramatically affect convergence of the ROM, is related to the numerical techniques used to solve the p2D DFN model. The use of mixed finite element methods in the FOM (resulting from the introduction of the exchange current, j_{Li} , as a problem variable) allows for the modes of j_{Li} to be obtained from two sources: the left singular vectors corresponding to the variable j_{Li} in the FOM itself, and the evaluation of the Butler-Volmer kinetics expression using the remaining variables of the problem and leading to a set of left singular vectors $f_{j_{Li}}$. As it has been shown, the latter approach is the most robust for solving the ROM. On the other hand, the selection of good error estimators is a crucial ingredient for building an efficient time-adaptive ROM. We extend the first approach based on local residuals in Ref. 17 by implementing an inexpensive strategy using implicit *a posteriori* error estimators, which overcomes the difficulties that prevent the correlation of local errors with residuals, and can be included in an automatic ROM-adaptation device. Thus, the presented low-cost error estimation approach within the time-adaptive strategy constitutes a key feature regarding the industrial applicability of the model. Finally, the results obtained for various scenarios having different charge/discharge C-rates, ranging from constant values up to 5C to a hybrid case with rates up to 2C, show that the proposed time-adaptive methodology is efficient, robust and provides accurate results for both cell voltages and internal variables. The analysis, as well as the clarification of the critical aspects of the p2D DFN model, show the time-adaptive strategy presented in this article to be a clear step forward with respect to the available results in the literature obtained from pre-processed ROMs and, to the best of our knowledge, is the first time such an adaptive method has been applied to electrochemical problems.

Although the development of this technique has been implemented in the p2D DFN model, all the analysis carried out is perfectly applicable to the p4D case, where the benefits of a reduction in the number of DOFs is even more self-evident and therefore the speed-up factor increases significantly, as shown by the results presented for a p4D implementation. On the other hand, in the framework of cell optimisation tasks, time-adaption techniques can be combined with parameter-adaption ones in order to further speed-up numerical simulation through model order reduction techniques. As optimisation proceeds, derived ROMs will need less updates from the FOM (since more information from the model is available from previous simulations) and the total computational cost of the optimisation process is expected to be comparable to the computational cost of a cell simulation using the FOM, making cell optimisation based on detailed p4D models affordable.

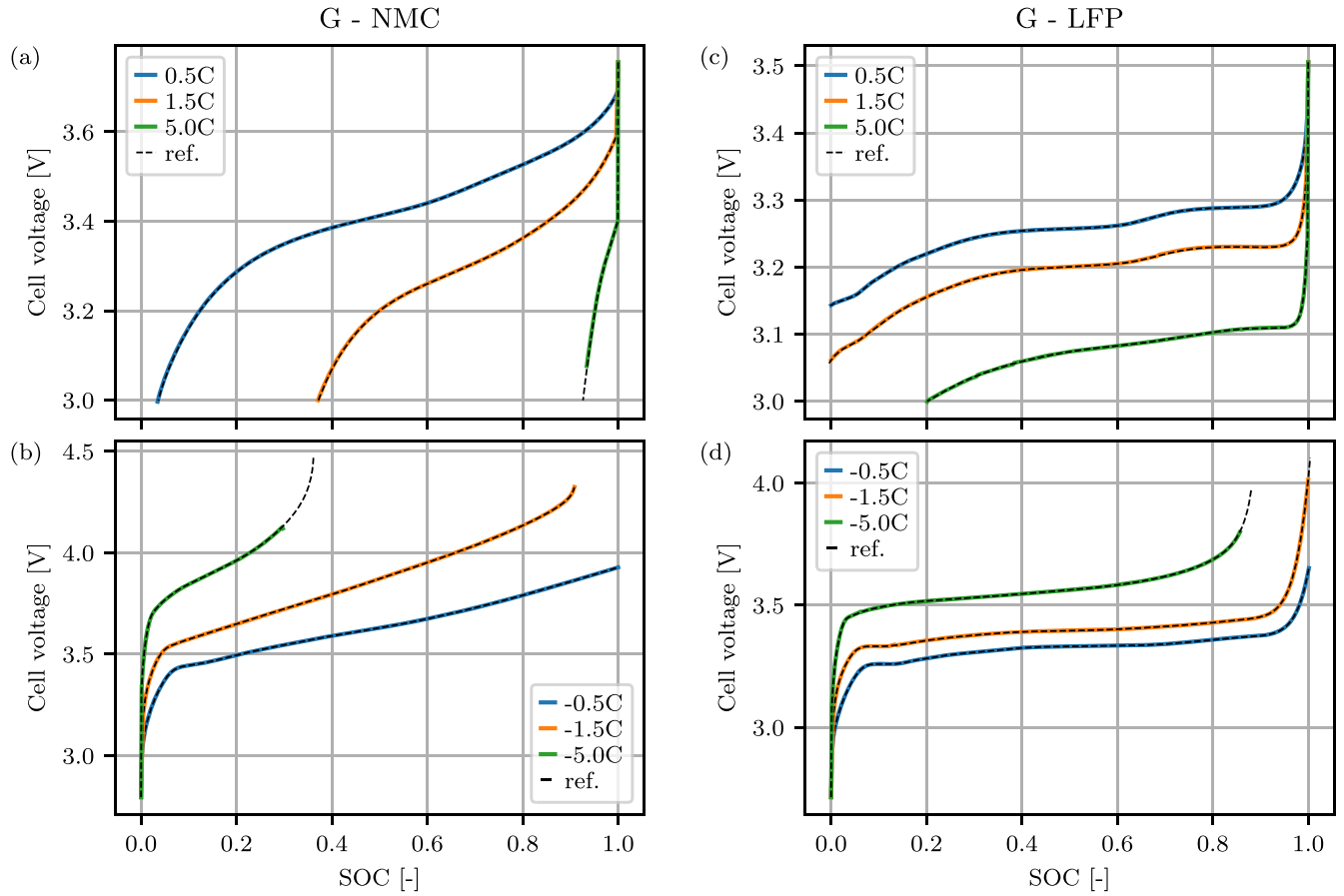


Figure 12. Voltage curves as a function of the cell state-of-charge (SOC) of the p2D time-adaptive ROM simulations for G-NMC and G-LFP cells at different discharge (positive) and charge (negative) C-rates.

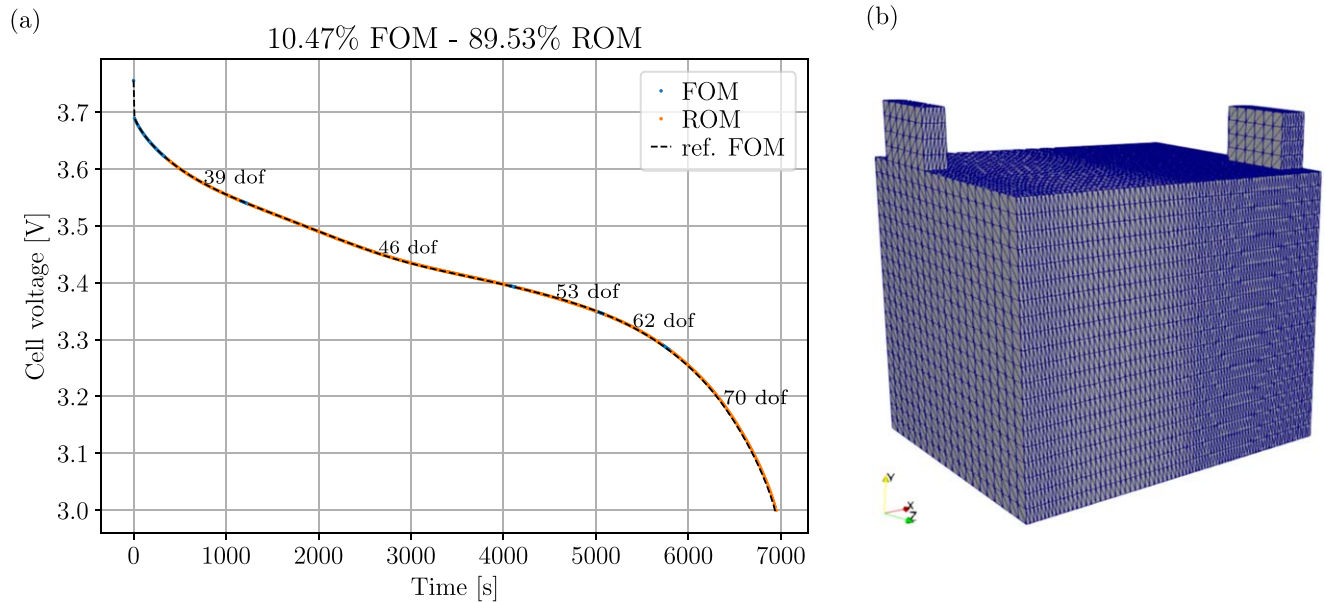


Figure 13. Voltage curve of the p4D time-adaptive ROM simulation of a G-NMC micro-cell at a constant 0.5C discharge rate (a) and 3D representation of the domain discretisation (b).

Two software tools have been developed by the authors implementing such techniques for p4D cell models: *echROM* for the acceleration of the numerical simulation using a time-adaptive ROM, and *OptiBat* for the implementation of cell optimisation algorithms using time- and parameter-adaptive ROMs. Both tools

are distributed using a Free Open Source Software (FOSS) license and are available at <https://defacto-project.eu/time-adaptive-reduced-p4d-tool/> and <https://defacto-project.eu/defacto-rom-optimisation-tool/>, respectively. Currently, in addition to the application of the

developed tools to the optimisation of the design of a real cell, some improvements for these tools are being considered. In particular, the use of a global error estimator instead of local error estimators (making unnecessary the calibration step explained in the paper) and the implementation of some alternatives concerning the stabilisation of the ROM will be included in future software releases.

Acknowledgments

This work has been funded by the European Union's Horizon 2020 research and innovation programme under grant agreement No 875247 (DEFACTO).

We thank J. L. Gutiérrez, for assistance with the simulation and post processing of the results presented in Fig. 7 and Table II. We also thank our colleagues from CIDETEC, who provided the reference full order model that greatly assisted the research.

Appendix A. POD-based ROM Formulation

• In the matrix form of the charge conservation in the solid phase equation, each $k_{ji}^{\phi_s}$ element of the $K_{\phi_s} \in \mathbb{R}^{N_{\phi_s} \times N_{\phi_s}}$ matrix is computed as

$$k_{ji}^{\phi_s} = \int_{\Omega} \sigma_{eff} \frac{d\psi_i^{\phi_s}}{dx} \frac{d\psi_j^{\phi_s}}{dx} dx,$$

each $a_{ji}^{\phi_s, jLi}$ element of the $A_{\phi_s}^{jLi} \in \mathbb{R}^{N_{\phi_s} \times N_{jLi}}$ matrix is

$$a_{ji}^{\phi_s, jLi} = \int_{\Omega} a_s F \psi_i^{jLi} \psi_j^{\phi_s} dx,$$

and each $b_j^{\phi_s}$ element of the $\mathbf{b}_{\phi_s} \in \mathbb{R}^{N_{\phi_s} \times 1}$ vector is

$$b_j^{\phi_s} = -i_{app} \psi_j^{\phi_s} |_{x=L}.$$

• In the matrix form of the charge conservation equation in the electrolyte, each $k_{ji}^{\phi_e}$ element of the $K_{\phi_e} \in \mathbb{R}^{N_{\phi_e} \times N_{\phi_e}}$ matrix is computed as

$$k_{ji}^{\phi_e} = \int_{\Omega} \kappa_{eff} \frac{d\psi_i^{\phi_e}}{dx} \frac{d\psi_j^{\phi_e}}{dx} dx,$$

and each $a_{ji}^{\phi_e, jLi}$ element of the $A_{\phi_e}^{jLi} \in \mathbb{R}^{N_{\phi_e} \times N_{jLi}}$ matrix is

$$a_{ji}^{\phi_e, jLi} = - \int_{\Omega} a_s F \psi_i^{jLi} \psi_j^{\phi_e} dx.$$

The matrix $B_{\phi_e}^{c_e} \in \mathbb{R}^{N_{\phi_e} \times N_{\beta_{ce}}}$ is defined as

$$B_{\phi_e}^{c_e} = C_{\phi_e}^{c_e} \tilde{\Xi}_{c_e}^{-1}$$

where $\tilde{\Xi}_{c_e}^{-1} \in \mathbb{R}^{N_{\beta_{ce}} \times N_{\beta_{ce}}}$ and each $c_{ji}^{\phi_e, c_e}$ element of the matrix $C_{\phi_e}^{c_e} \in \mathbb{R}^{N_{\phi_e} \times N_{\beta_{ce}}}$ is computed as

$$c_{ji}^{\phi_e, c_e} = \int_{\Omega} \kappa_{D, eff} \xi_i^{c_e} \frac{d\psi_j^{\phi_e}}{dx} dx.$$

• In the matrix form of the mass conservation equation in the solid phase, each $m_{ij}^{c_s}$ element of the $M_{c_s} \in \mathbb{R}^{N_{c_s} \times N_{c_s}}$ matrix is computed as

$$m_{ij}^{c_s} = \sum_{k=1}^{N_r^*} \sum_{l=1}^{N_r^*} \int_{\Omega} \int_{\Omega_r} r^{*2} \psi_{i,j}^{c_s} \psi_i^{r^*} \psi_{k,l}^{c_s} \psi_k^{r^*} dr^* dx,$$

each $k_{ij}^{c_s}$ element of the $K_{c_s} \in \mathbb{R}^{N_{c_s} \times N_{c_s}}$ matrix is computed as

$$k_{ij}^{c_s} = \sum_{k=1}^{N_r^*} \sum_{l=1}^{N_r^*} \int_{\Omega} \int_{\Omega_r} \frac{D_s}{R_s^2} r^{*2} \psi_{i,j}^{c_s} \frac{d\psi_i^{r^*}}{dr^*} \psi_{k,l}^{c_s} \frac{d\psi_k^{r^*}}{dr^*} dr^* dx$$

and each $a_{li}^{c_s, jLi}$ element of the $A_{c_s}^{jLi} \in \mathbb{R}^{N_{c_s} \times N_{jLi}}$ matrix is computed as

$$a_{li}^{c_s, jLi} = \sum_{k=1}^{N_r^*} \int_{\Omega} \frac{1}{R_s} \psi_i^{jLi} \psi_{k,l}^{c_s} \psi_k^{r^*} |_{r^*=1} dx.$$

• In the matrix form of the mass conservation equation in the electrolyte, each $m_{ji}^{c_e}$ element of the matrix $M_{c_e} \in \mathbb{R}^{N_{c_e} \times N_{c_e}}$ is computed as

$$m_{ji}^{c_e} = \int_{\Omega} \epsilon_e \psi_i^{c_e} \psi_j^{c_e} dx,$$

each $k_{ji}^{c_e}$ element of the matrix $K_{c_e} \in \mathbb{R}^{N_{c_e} \times N_{c_e}}$ is computed as

$$k_{ji}^{c_e} = \int_{\Omega} D_{e, eff} \frac{d\psi_i^{c_e}}{dx} \frac{d\psi_j^{c_e}}{dx} dx,$$

and, finally, each $a_{ji}^{c_e, jLi}$ element of the matrix $A_{c_e}^{jLi} \in \mathbb{R}^{N_{c_e} \times N_{jLi}}$ is given by

$$a_{ji}^{c_e, jLi} = - \int_{\Omega} a_s (1 - t_+^0) \psi_i^{jLi} \psi_j^{c_e} dx.$$

• In the matrix form of the Butler-Volmer kinetics equation, each k_{ji}^{jLi} element of the matrix $K_{jLi} \in \mathbb{R}^{N_{jLi} \times N_{jLi}}$ is computed as

$$k_{ji}^{jLi} = \int_{\Omega} \psi_i^{jLi} \psi_j^{jLi} dx,$$

and the matrix $B_{jLi}^{jLi} \in \mathbb{R}^{N_{jLi} \times N_{\beta_{jLi}}}$ is defined as

$$B_{jLi}^{jLi} = C_{jLi}^{jLi} \tilde{\Xi}_{jLi}^{-1}$$

where $\tilde{\Xi}_{jLi}^{-1} \in \mathbb{R}^{N_{\beta_{jLi}} \times N_{\beta_{jLi}}}$ and each $c_{ji}^{jLi, jLi}$ element of the matrix $C_{jLi}^{jLi} \in \mathbb{R}^{N_{jLi} \times N_{\beta_{jLi}}}$ is computed as

$$c_{ji}^{jLi, jLi} = - \int_{\Omega} \xi_i^{jLi} \psi_j^{jLi} dx.$$

Appendix B. G-NMC and G-LFP cell and simulation parameters

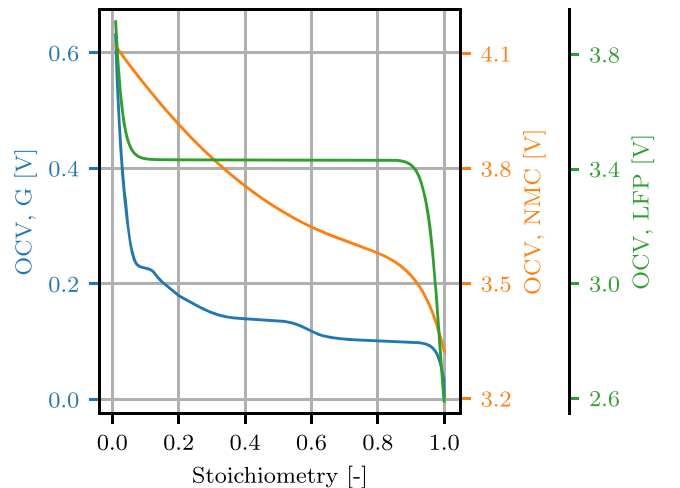


Figure B.1. Open circuit voltage curves for the active materials G,²⁴ NMC²⁵ and LFP.²⁷

Table B-1. Electrode parameters. *G-NMC cell, †G-LFP cell.

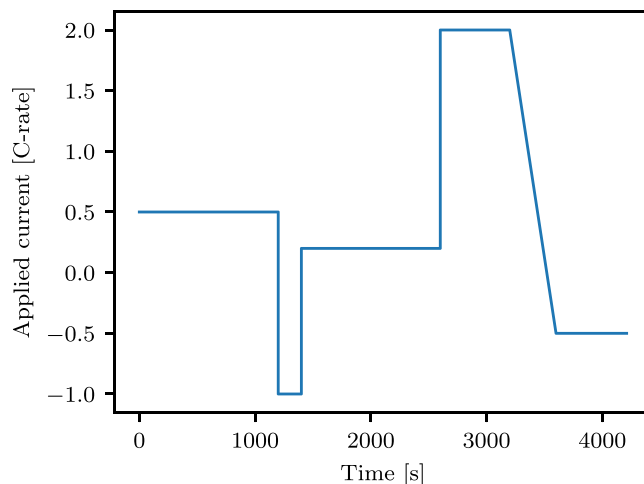
Parameter	Unit	G ²⁴ ($k = a$)	NMC ^{25,26} ($k = c$)	LFP ^{27,28} ($k = c$)
L_k	m	$9 \cdot 10^{-5}$ *; $5 \cdot 10^{-5}$ †	$5.4 \cdot 10^{-5}$	$9.25 \cdot 10^{-5}$
S	m ²	$1 \cdot 10^{-2}$	$1 \cdot 10^{-2}$	$1 \cdot 10^{-2}$
ε_e	—	0.33	0.335	0.332
γ	—	2.914	2.43	1.5
σ_{eff}	S/m	31.13	$6.679 \cdot 10^{-2}$	$2.730 \cdot 10^{-1}$
κ_{eff}	S/m	$4.721 \cdot 10^{-2}$	$8.375 \cdot 10^{-2}$	$2.285 \cdot 10^{-1}$
$\kappa_{D,eff}$	A/m	$-1.377 \cdot 10^{-3}$	$-2.443 \cdot 10^{-3}$	$-6.665 \cdot 10^{-3}$
R_s	m	$5 \cdot 10^{-6}$	$5.22 \cdot 10^{-6}$	$3.65 \cdot 10^{-8}$
SOC _{k,1}	—	0.84	0.2661	0.03
SOC _{k,0}	—	0.0065	0.9084	0.76
k_0	m ^{2.5} /(mol ^{0.5} s)	$1 \cdot 10^{-11}$	$3.54 \cdot 10^{-11}$	$1.4 \cdot 10^{-12}$
$c_{s,max}$	mol/m ³	28700	51765	22806
D_s	m ² /s	$3.9 \cdot 10^{-14}$	$1.48 \cdot 10^{-15}$	$1.18 \cdot 10^{-18}$
U_{ocv}	V		Fig. B-1	

Table B-2. Separator and electrolyte parameters.

Parameter	Unit	Value
D_e	m ² /s	$3.222 \cdot 10^{-10}$
κ	S/m	1.1943
t_+^0	—	0.38
$c_{e,0}$	mol/m ³	1000

(a) LiPF₆ electrolyte.²⁹

Parameter	Unit	Value
L_s	m	$1.2 \cdot 10^{-5}$
S	m ²	$1 \cdot 10^{-2}$
γ	—	2.57
ε_e	—	0.47
κ_{eff}	S/m	$1.716 \cdot 10^{-1}$
$\kappa_{D,eff}$	S/m	$-5.005 \cdot 10^{-3}$

(b) Separator.²⁵**Figure B-2.** Applied current of the hybrid load cycle.**Table B-3. Simulation parameters.**

Description	Symbol	Units	Value (baseline case)	Value (hybrid cycle)
Simulation time	t_{sim}	s	7200	4200
Time step	Δt	s	10	5
Applied current	I_{app}	C-rate	0.5	Fig. B-2
Minimum voltage	V_{min}	V	3	3
Elements per subdomain	N	—	30	30
Temperature	T	K	298.15	298.15
Initial cell SOC	SOC ₀ ^{cell}	—	1	1

ORCID

Eduardo Jané <https://orcid.org/0000-0003-2848-3406>
 Ruth Medeiros <https://orcid.org/0000-0003-2444-5832>
 Fernando Varas <https://orcid.org/0000-0003-0267-1011>
 María Higuera <https://orcid.org/0000-0001-7452-6302>

References

- M. Smith, R. E. García, and Q. C. Horn, *J. Electrochem. Soc.*, **156**, A896 (2009).
- A. Latz and J. Zausch, *J. Power Sources*, **196**, 3296 (2011).
- S. Hein and A. Latz, *Electrochim. Acta*, **201**, 354 (2016).
- J. Feinauer, S. Hein, S. Rave, S. Schmidt, D. Westhoff, J. Zausch, O. Iliev, A. Latz, M. Ohlberger, and V. Schmidt, *J. Comput. Sci.*, **31**, 172 (2019).
- M. Doyle, T. F. Fuller, and J. Newman, *J. Electrochem. Soc.*, **140**, 1526 (1993).
- B. S. Haran, B. N. Popov, and R. E. White, *J. Electrochem. Soc.*, **145**, 4082 (1998).
- X. Han, M. Ouyang, L. Lu, and J. Li, *J. Power Sources*, **278**, 802 (2015).
- V. R. Subramanian, V. Boovaragavan, and V. D. Diwakar, *Electrochem. Solid-State Lett.*, **10**, A255 (2007).
- X. Li, G. Fan, G. Rizzoni, M. Canova, C. Zhu, and G. Wei, *Energy*, **116**, 154 (2016).
- N. Tran, M. Vilathgamuwa, T. Farrell, S. S. Choi, Y. Li, and J. Teague, *J. Electrochem. Soc.*, **165**, A1409 (2018).
- Z. Khalik, M. Donkers, and H. Bergveld, *J. Power Sources*, **488**, 229427 (2021).
- M. A. Kehs, M. D. Beeney, and H. K. Fathy, "Computational efficiency of solving the DFN battery model using descriptor form with Legendre polynomials and Galerkin projections." *2014 American Control Conference* 260 (2014).
- B. Bhikkaji and T. Söderström, *Int. J. Control*, **74**, 1543 (2001).
- L. Cai and R. E. White, *J. Electrochem. Soc.*, **156**, A154 (2009).
- L. Xia, E. Najafi, Z. Li, H. Bergveld, and M. Donkers, *Appl. Energy*, **208**, 1285 (2017).
- S. Kosch, Y. Zhao, J. Sturm, J. Schuster, G. Mulder, E. Ayerbe, and A. Jossen, *J. Electrochem. Soc.*, **165**, A2374 (2018).

17. M. L. Rapún, F. Terragni, and J. M. Vega, *Int. J. Numer. Methods Eng.*, **104**, 844 (2015).
18. C. Johnson, *Numerical Solution of Partial Differential Equations by the Finite Element Method* (Dover Publications) (2012), Dover Books on Mathematics Series (Incorporated).
19. G. Berkooz, P. Holmes, and J. L. Lumley, *Annu. Rev. Fluid Mech.*, **25**, 539 (1993).
20. L. Sirovich, *Q. Appl. Math.*, **45**, 561 (1987).
21. D. Boffi, F. Brezzi, and M. Fortin, *Mixed Finite Element Methods and Applications* (Springer, Berlin) (2013).
22. M. Ainsworth and J. T. Oden, *Comput. Methods Appl. Mech. Engrg.*, **142**, 1 (1997).
23. R. C. Aylagas, C. Ganuza, R. Parra, M. Yañez, and E. Ayerbe, *J. Electrochem. Soc.*, **169**, 090528 (2022).
24. B. Rieger, S. V. Erhard, K. Rumpf, and A. Jossen, *J. Electrochem. Soc.*, **163**, A1566 (2016).
25. C. H. Chen, F. B. Planella, K. O'Regan, D. Gastol, W. D. Widanage, and E. Kendrick, *J. Electrochem. Soc.*, **167**, 080534 (2020).
26. I. Baccouche, S. Jemmali, B. Manai, N. Omar, and N. E. B. Amara, *Energies*, **10**, 764 (2017).
27. Y. Ye, Y. Shi, and A. A. Tay, *J. Power Sources*, **217**, 509 (2012).
28. M. Safari and C. Delacourt, *J. Electrochem. Soc.*, **158**, A562 (2011).
29. L. O. Valøen and J. N. Reimers, *J. Electrochem. Soc.*, **152**, A882 (2005).